Contents

1 Theoretical Background

In this section we introduce the theoretical background needed to perform this experiment. Furthermore a minimal description of the Standard Model of particle physics is given and a brief review of some basic features of scattering processes described by quantum field theories (QFTs) are discussed using an analogy to non-relativistic quantum mechanics. We start by a short review of point particle kinematics used within this experiment.

1.1 Point Particle Kinematics

Since the goal of particle physics is to study matter at the smallest scales, extremely high energies are needed. This statement can be motivated by a simple resolution argument: To resolve very small objects one needs a sufficiently small wavelength. Hence, in a scattering experiment we resolve smaller scales with higher momenta (and therefore higher energies) as the de Broglie wavelength goes as $\lambda = h/p$.

The theory which needs to be applied at high energies and flat space-time[1] is special relativity. Throughout this work we will use the $(+,-,-,-)$-signature for the Minkowski metric, where the 0th entry accounts for the time dimension. We will also use natural units where $c = 1$. For point particle kinematics the object of interest is the four-momentum vector

$$\boldsymbol{p} = \begin{pmatrix} E \\ p_x \\ p_y \\ p_z \end{pmatrix}, \tag{1}$$

which satisfies the on-shell condition

$$\boldsymbol{p}_\mu \boldsymbol{g}^{\mu\nu} \boldsymbol{p}_\nu = \boldsymbol{p}_\mu \boldsymbol{p}^\mu = E^2 - \vec{p}^2 = m^2, \tag{2}$$

where $\vec{p}$ is the usual three-momentum and m is the invariant mass which is Lorentz invariant. For later analysis it is also practical to define the transverse mass

$$m_{\mathrm{T}} = \sqrt{2 p_{\mathrm{T}}(e) p_{\mathrm{T}}(\nu)(1 - \cos(\phi_e - \phi_\nu))}, \tag{3}$$

which is invariant under Lorentz boosts along the z-axis (beam-axis). The transverse momentum is just the transverse proportion of the momentum with respect to the z-axis. It is often useful to reparameterize a problem using coordinates which satisfy certain symmetries. Therefore cylindrical coordinates are used when dealing with colliding-beam-experiments, since the differential cross section respects the cylindrical symmetry of the initial state. Hence one of the most important parameters of a particles trajectory is the polar angle θ, which is the angle between the trajectory and the beam axis. Instead of using θ directly it is of practical use to define the pseudo-rapidity

$$\eta = -\ln\left[\tan\left(\frac{\theta}{2}\right)\right], \tag{4}$$

[1] This assumption holds since on small scales space-time is sufficiently flat.

which is a dimensionless parameter. Using high energy approximations (neglecting rest-masses), it is possible to reexpress the transverse momentum in terms of the pseudorapidity η and the measured energy E of the particle via

$$p_T \approx \frac{E}{\cosh \eta},$$

this expression is intensively used and a derivation of which is found in appendix A.

1.2 Particle Scattering Processes in QFTs

We already stated that due to the high energies needed to explore the realm of fundamental particles the applied theory needs to satisfy the laws of special relativity. It is also not surprising that a theory of fundamental particles needs to obey the features of quantum mechanics. From the unification of both of these concepts quantum field theories (QFTs) arise in a quite natural way.

When exploring the interactions of fundamental particles via scattering experiments, it is clear to see that the scattering matrix is the most central object in this context. The scattering matrix relates the initial state and the final state of a physical system involved in a scattering process, and its interpretation is quite similar to the scattering matrix in non-relativistic quantum mechanics. The scattering matrix contains the matrix elements which need to be computed to make predictions about scattering events. Although the construction of analytical expressions for the matrix elements, which can be evaluated numerically, can be quite complex, the perturbative expansion of them has a pictorial representation. These pictorial representations are called Feynman diagrams, which can be used to build a good intuition on what is going on. It might be useful to look at a simple example. In fig. 1 two Feynman diagrams are shown. These diagrams correspond to a scattering event where one electron and one positron are in the initial and final states, so we have the reaction $e^+e^- \to e^+e^-$. It is seen that we can choose different "paths" from the initial state to the final state. In fig. 1 for example the interaction is once "mediated" by a virtual photon and once by a virtual Z-boson. The four-momenta of these virtual particles[2]do not respect the on-shell condition shown in eq. (2).

A useful way to think about these Feynman diagrams is as an analogy to the propagation probabilities in non-relativistic quantum mechanics. From non-relativistic quantum mechanics we know that we cannot assign a trajectory to a particle which propagates from one point to another, but every path connecting the initial and final position has a probability assigned to it. The same reasoning applies to some extend to Feynman diagrams. The outer lines of a Feynman diagram dictate the initial and final state of the system, whereas the propagator (the virtual particle) is a "trajectory" connecting the initial and the final state, to which a probability is assigned. Another similarity is that in non-relativistic quantum mechanics the classical trajectory contributes the most to the propagator. This also holds to some extend for the QFT calculations. The probability for a specific

[2]It has to be pointed out that the term virtual particle has lead to a lot of confusion, even amongst physicists. There is no reason to assume that the virtual particle shown in a Feynman diagram like fig. 1 really existed as a particle. After all a Feynman diagram is a pictorial representation of a perturbative expansion of the corresponding matrix element and interpretations like the ones discussed in this protocol are often oversimplifying the underlying theory.

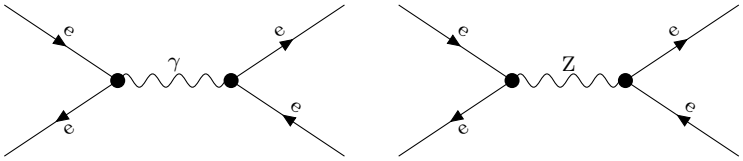

Figure 1: In this picture two examples for tree level Feynman diagrams are shown, where one electron and one positron are in the initial and final states (in general 6 more diagrams contribute to this process at tree level in Feynman-t'Hooft-gauge using the Standard Model vertices.). In this work we will use the convention where the arrow of time points from left to right. (So in this figure only annihilation processes are shown.)

tree-level particle reaction is maximal [3] when the propagator (virtual particle) is close to on-shell. This maximum in contribution causes the resonance when the kinematics of the initial particles allow the propagator to be close to on-shell. This analogy follows very naturally from the path integral formalism. For a rigorous treatment we suggest the books by Sakurai and Peskin [9, 8].

This reasoning is heavily used when applying cuts to the data, since if we are interested in a single resonance of the system and we have a rough idea of where this resonance is expected[4], we can use the knowledge of the final state (the particles and their properties) and its kinematic parameters to select events which might be amplified by the resonance of the new particle. And we can also use these ideas to suppress events which might contribute to the background.

1.3 The Standard Model

The Standard Model of particle physics is a quantized gauge theory with the underlying gauge group

$$\mathrm{SU}(3) \times \mathrm{SU}(2) \times \mathrm{U}(1). \tag{5}$$

To each of the group generators there is a gauge boson. So for the strong interaction we have, due to the SU(3) gauge group, $3^2 - 1 = 8$ generators and hence 8 different gluons. It is noticeable that this is the reason there is no colorless gluon. For the weak interaction we have, due to the SU(2) gauge group, $2^2 - 1 = 3$ generators and hence 3 gauge bosons, which can be roughly identified by the $\mathrm{W}^{\pm}$- and Z-Bosons. The electromagnetic interaction is a U(1) gauge theory hence there is only one gauge boson, which is roughly identified by the photon.[5] These gauge bosons are the mediators of the weak, strong and electromagnetic forces. The gravitational force is not described within the Standard Model. These forces act between the fermions[6] of the Standard Model which are listed

[3] Of course the contribution of a single Feynman diagram to the total scattering amplitude depends on the perturbative order (roughly the number of vertices) and the couplings involved in the event of interest. But the contribution of a single diagram also depends on the initial kinematics of the scattering process. So for tree-level processes we get a resonance whenever the propagator (virtual particle) goes on-shell.

[4] The search for a sensible mass window for an additional particle is very intriguing but exceeds the scope of this protocol.

[5] Due to the spontaneous symmetry breaking of the Higgs field the direct identification of the γ, Z and $\mathrm{W}^{\pm}$ bosons is a little more subtle than presented here. A good introduction to the topic is presented in the book of Böhm, Denner and Joos [6].

[6] Particles of half integer spin, in the case of the fundamental fermions of the Standard Model all fermions have spin-1/2.

in fig. 2. The quarks interact via all three interactions, whereas the charged leptons interact via

Charged Leptons Neutrinos	$\begin{pmatrix} \mathrm{e} \\ \nu_e \end{pmatrix}_1 \begin{pmatrix} \mu \\ \nu_\mu \end{pmatrix}_2 \begin{pmatrix} \tau \\ \nu_\tau \end{pmatrix}_3$
Uptype Quarks Downtype Quarks	$\begin{pmatrix} \mathrm{u} \\ \mathrm{d} \end{pmatrix}_1 \begin{pmatrix} \mathrm{c} \\ \mathrm{s} \end{pmatrix}_2 \begin{pmatrix} \mathrm{t} \\ \mathrm{b} \end{pmatrix}_3$

Figure 2: The fermions of the Standard Model of particle physics ordered by particle type (same type horizontal) and generation $i \in \{1, 2, 3\}$ (indicated by subscripts)

the weak and the electromagnetic forces and the neutrinos interact exclusively via the weak force. The last particle of the Standard Model is the Higgs boson. The Higgs boson is described by a scalar field and therefore has spin-0. The Higgs boson is not charged. Since direct mass terms for the massive gauge bosons would violate gauge symmetry the Higgs boson is needed to generate the mass of the massive gauge Bosons. Additionally the fermions of the Standard Model get their mass by the Higgs boson, too.

1.4 The Higgs Mechanism

Since it is observed by experiments that the gauge bosons of the weak interaction must be massive, one of the main tasks for a consistent description of nature is to generate masses for the $Z, W^{\pm}$ bosons keeping gauge invariance unbroken, while the photon should remain massless. A naive approach would be to add mass terms to the Lagrangian. A free field Lagrangian for a spin-1 boson including a mass term would be

$$\mathcal{L}_{\text{Proca}} = -\frac{1}{4} F_{\mu\nu} F^{\mu\nu} + m^2 A_\mu A^\mu. \tag{6}$$

Such a Lagrangian does not respect gauge invariance, therefore this approach would not yield the desired results.

The solution to this problem is the Higgs mechanism. For this purpose a complex scalar doublet Φ, which transforms in the fundamental representation under $SU(2)_{\text{W}}$ transformations, is introduced

$$\Phi(x) = \begin{pmatrix} \phi^+(x) \\ \phi^0(x) \end{pmatrix}, \tag{7}$$

where ϕ^+, ϕ^0 are complex scalar fields. Without further specification this doublet has four real degrees of freedom. The corresponding Lagrangian for this doublet is

$$\mathcal{L}_{\text{Higgs}} = (D_\mu \Phi)^\dagger (D^\mu \Phi) + \mu^2 \Phi^\dagger \Phi - \frac{\lambda}{4} (\Phi^\dagger \Phi)^2, \tag{8}$$

where D_μ is the covariant derivative specified by the gauge group of the Standard Model. This Lagrangian contains two free parameters μ, λ, where μ is a mass parameter for the Higgs doublet and λ is a coupling constant for the self-interaction of the Higgs doublet. For a single complex scalar

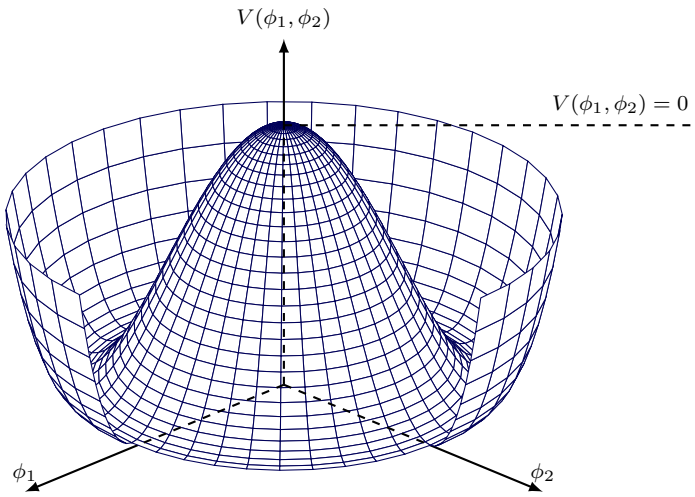

Figure 3: Higgs potential depending on the field components ϕ_1, ϕ_2 of a single scalar field $\phi = \phi_1 + i\phi_2$ where the parameter μ is restricted to $\mu^2 > 0$ so that the potential has a degenerate minimum, and the parameter λ is restricted to $\lambda > 0$ so its bounded from below. Furthermore, it can be seen that the vacuum expectation value for the field is non–vanishing, imposed by the local minima.

field, the potential of the field configuration can be illustrated by fig. 3. To guarantee vacuum stability it is of course necessary that the potential is bounded from below, since otherwise the field configuration would just decay into lower and lower energy configurations. This property is ensured by $\lambda > 0$, as shown in the example given in fig. 3.

The field configuration minimizing the potential [7]

$$V(\Phi^\dagger\Phi) = -\mu^2\Phi^\dagger\Phi + \frac{\lambda}{4}(\Phi^\dagger\Phi)^2 \tag{9}$$

which is given by

$$|\Phi_0|^2 = \Phi_0^\dagger\Phi_0 = \frac{2\mu^2}{\lambda} =: \frac{v^2}{2} \neq 0, \tag{10}$$

where we introduced the parameter v, is not unique, since the minimum is only restricted by the norm of the doublet. It is therefore only defined up to a phase, so one is thus free to choose a phase since all the field configurations minimizing the potential are physically equivalent[8].

Since it is inconvenient to quantize a field with non-zero vacuum expectation value, we need to shift the fields, such that we can quantize the shifted fields. So the Higgs doublet is reexpressed by fields with zero vacuum expectation value. This reparameterization is given by

$$\Phi(x) = \begin{pmatrix} 0 \\ \frac{v}{\sqrt{2}} \end{pmatrix} + \begin{pmatrix} \phi^+(x) \\ \frac{1}{\sqrt{2}}(h(x) + i\chi(x)) \end{pmatrix} = \Phi_0 + \Phi_1(x), \tag{11}$$

[7] The field configuration minimizing the potential also minimizes the total energy, since the kinetic energy cannot be negative and thus to be minimal must be zero, which is given for a field configuration, which is constant in space-time.

[8] For a simple illustration of this property one can once again look at fig. 3.

where $h(x)$ and $\chi(x)$ are real scalar fields and $\phi^+(x)$ is a complex scalar field and the representation of the vacuum expectation value of the Higgs doublet is chosen as

$$\langle\Phi\rangle = \langle 0|\Phi|0\rangle = \Phi_0 = \begin{pmatrix} 0 \\ \frac{v}{\sqrt{2}} \end{pmatrix}. \tag{12}$$

For a phenomenological discussion of the Higgs doublet it is useful to choose another configuration space parametrization. In fig. 3 it is somewhat obvious that one is able to choose a polar parametrization for the single complex scalar field $\phi(x)$ shown in the figure. The same arguments apply for the Higgs doublet Φ, although other than in fig. 3, the Higgs doublet is not a single complex field but two of them. The polar representation for the Higgs doublet is given by

$$\Phi(x) = \exp\left(i\frac{\theta^j(x)I^j}{v}\right)\begin{pmatrix} 0 \\ \frac{1}{\sqrt{2}}(v+h(x)) \end{pmatrix}, \tag{13}$$

where the I^j are the generators of the SU(2) gauge group[9]. By choosing a proper gauge for the field in eq. (13) the phase factor in eq. (13) is canceled by the choice of the gauge. This gauge choice is called unitary gauge. One then concludes that out of the four degrees of freedom of the Higgs doublet only one is physical. This physical degree of freedom is identified as the Higgs boson field.

The kinetic term for the Higgs doublet then introduces the term $(D_\mu\Phi_0)^\dagger(D_\mu\Phi_0)$ to the Lagrangian[10], which introduces mass terms for the gauge fields. To be more precise one can expand the Lagrangian in eq. (8) in the unitary gauge, which yields

$$\begin{aligned}\mathcal{L}_{\text{Higgs}} =& \frac{1}{2}(\partial_\mu h)(\partial^\mu h) - \mu^2 h^2 \\ &+ \frac{v^2}{8}\left(g_2^2 W_\mu^1 W^{1,\mu} + g_2^2 W_\mu^2 W^{2,\mu} + \left(g_2 W_\mu^3 + g_1 B_\mu\right)\left(g_2 W^{3,\mu} + g_1 B^\mu\right)\right) \\ &+ \mathcal{L}_{\text{Int.}}(h, W^a, B),\end{aligned} \tag{14}$$

where the terms bilinear in the gauge fields W^1, W^2, W^3, B are the desired mass terms. Realizing that there are terms in the Lagrangian that are proportional to $W_\mu^3 B^\mu$, one can already conclude that the fields W_μ^i and B_μ do not correspond to the mass eigenstates which are observed in experiments. The fields describing mass eigenstates of the particles are obtained by the transformations[11]

$$\begin{pmatrix} A_\mu \\ Z_\mu \end{pmatrix} = \begin{pmatrix} c_W & -s_W \\ s_W & c_W \end{pmatrix}\begin{pmatrix} B_\mu \\ W_\mu^3 \end{pmatrix}, \quad W_\mu^\pm = \frac{1}{\sqrt{2}}\left(W_\mu^1 \mp i W_\mu^2\right), \tag{15}$$

where the parameters are given by

$$c_W = \cos\theta_W := \frac{g_2}{\sqrt{g_1^2+g_2^2}}, \quad s_W = \sin\theta_W := \frac{g_1}{\sqrt{g_1^2+g_2^2}}. \tag{16}$$

[9] To build some intuition for the reparameterization in eq. (13) it is again useful to look at fig. 3. The θ fields can excite modes along the angular degree of freedom in configuration space, whereas the Higgs field h excites modes of the radial degree of freedom in configuration space.

[10] This seen by introducing eq. (13) into the Higgs Lagrangian, without the phase factor, since it was canceled by the gauge transformation.

[11] These transformations are just rotations in configuration space under which the Lagrangian is invariant and therefore do not change the physics described by the model.

The parameter θ_W is called weak mixing angle, sometimes also called Weinberg angle. Applying this redefinition of the fields to the Lagrangian one can read off the masses of the fields, which are then given by

$$M_W = \frac{g_2 v}{2}, \quad M_Z = \frac{v}{2}\sqrt{g_1^2 + g_2^2}, \quad M_A = 0, \quad M_h = \sqrt{2}\mu. \tag{17}$$

Since the gauge bosons are now massive, they have a longitudinal degree of freedom. Therefore the three massive gauge fields get one additional degree of freedom each. These additional degrees of freedom are exactly the three unphysical degrees of freedom of the Higgs doublet, which are now absorbed by the gauge bosons. The masses of the fermions of the Standard Model are generated via Yukawa couplings of the fermion fields and the Higgs field, which is done in a way that the Standard Model is parity violating, since this was observed by experiments by Wu [11].

To conclude this section about the Higgs mechanism we show the most important Higgs production mechanism and the Higgs decay mechanisms we used as a search channel. This is of great interest when applying the cuts for the Higgs search, since a good knowledge of the dominating Higgs production/decay channels gives the information about the measured final state (e.g. additional Jets apart from the final state of the actual Higgs decay, due to for example top fusion as an Higgs production event.). The most important Higgs production mechanisms are shown in fig. 4. The most dominant production mechanism is the gluon fusion process seen in the lower left of fig. 4. The search channel we use is shown in fig. 5. The four lepton decay is a good candidate for a search channel, since the final state should be detectable in a rather clean manner.

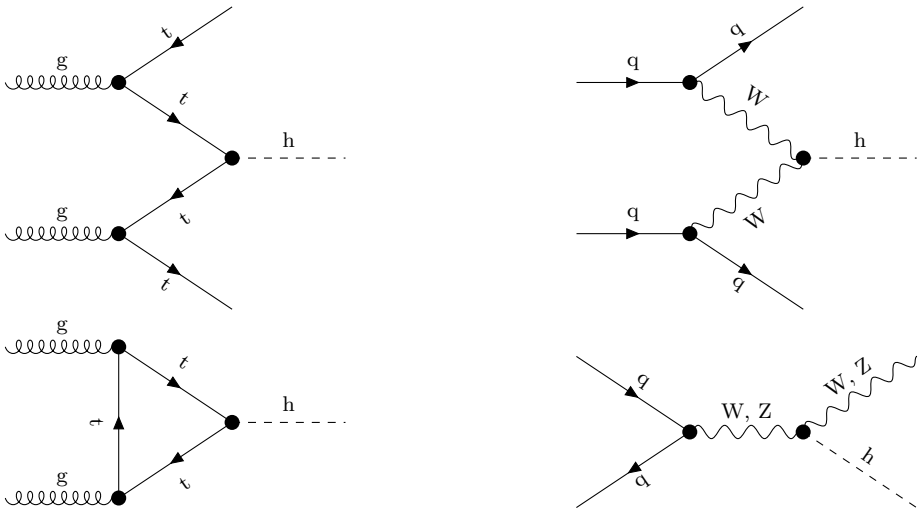

Figure 4: In this figure some of the most important Higgs productions mechanisms are displayed. (top fusion (upper left), vector boson fusion (upper right), gluon fusion (lower left), W, Z Bremsstrahlung (lower right))

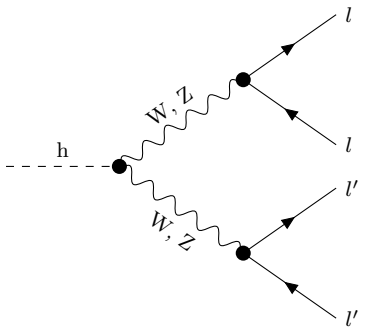

Figure 5: In this figure the Feynman diagram corresponding to the Higgs decay h → WW → $l\bar{l}\,l\bar{l}$, which was used as a search channel.

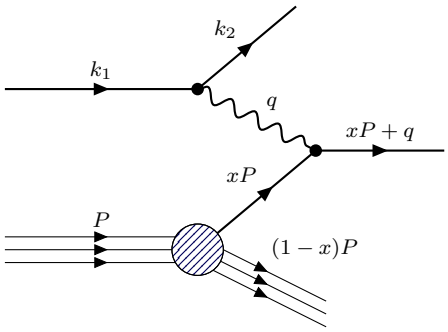

Figure 6: Scattering of an electron off a proton, where the proton has the initial four-momentum P and the electron has the initial four-momentum k_1. Within the naive parton model, the proton is described as a loosely bound cloud of partons. The electron in the figure scatters off such a parton by exchanging a photon.

1.5 The Parton Model

The naive parton model describes the proton as a weakly-bound system made of quasi-free and point-like particles, which are called partons. An explanatory example is the deep inelastic scattering of an electron and a proton. The process is visualized in fig. 6, where P is the initial four-momentum of the proton and k_1 is the initial four-momentum of the electron. It is assumed that the parton, which interacts with the electron, carries a definite fraction xP of the proton's four-momentum. These collisions are considered to happen at large center-of-mass energies, so that one can neglect the masses of the proton and the electron in the kinematics. Therefore, the proton has an almost light-like momentum along the axis of collision. It is assumed that the partons are collinear with the proton. This assumption is justified by the fact that at very large energies the interaction occurs almost instantly since the interaction time observed in the lab-frame is time-dialated. Therefore it is very unlikely that within this small time interval any interaction within the proton occurs, such that the parton gains additional transverse momentum. One concludes that the four-momentum of the parton is actually a longitudinal fraction of the protons four-momentum.

Hence, for a leading-order approximation, the cross section for the scattering process is given by the cross section of the electron–quark scattering $\hat{\sigma}$ at given longitudinal fraction x multiplied by the probability that the proton contains a quark with this fraction x, which is given by the parton distribution function $f_q(x)$, where it is integrated over all possible fractions $x \in (0, 1)$,

$$\sigma_{e^- p \to e^- X} = \int_0^1 \mathrm{d}x \sum_{q \in \{u,d,s,c,t,b\}} f_q(x)\, \hat{\sigma}_{e^- q \to e^- q} \tag{18}$$

1.6 The ATLAS-Detector

The ATLAS-detector consists out of four detectors that are designed for different purposes. In fig. 7 a sketch of the detector is shown and one can see ordered from the collision point to the outside the inner detector, the liquid argon calorimeter, the tile calorimeter and the muon spectrometer. In and around the detector the magnetic system consisting of the barrel toroids, the end-cap toroid and the central solenoid magnet is placed.

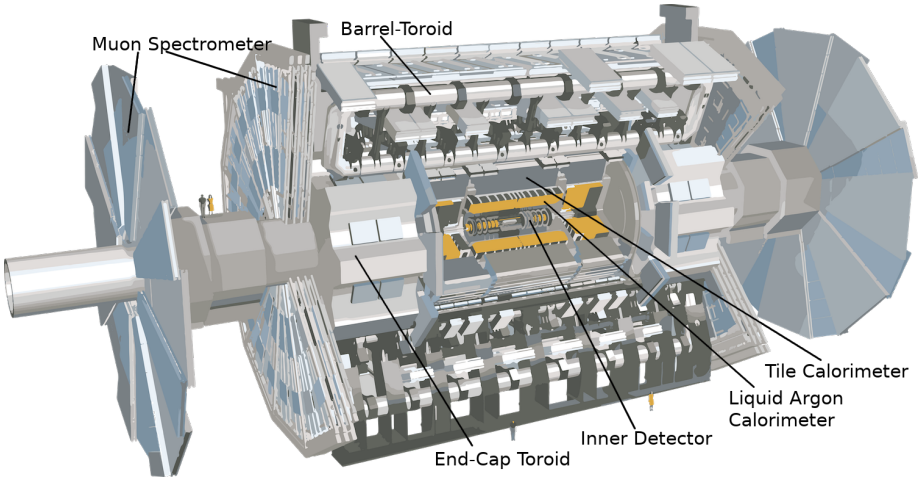

Figure 7: Sketch of the ATLAS-detector. Image taken from [2], labels were added.

The Inner Detector A closer look on the inner detector is given in fig. 8. The information about the inner detector was taken from [7, 5, 3].

The innermost layer of the inner detector is a semiconductor tracker, called Pixel detector. In four layers that are wrapped around the beam pipe and three disks in each end-cap 92 million silicon pixels are placed. The innermost layer has pixels with an area of $50 \cdot 250\mu\mathrm{m}$ and is specially designed to detect secondary vertices emerging from the decay of b-hadrons, its called insertable b-layer (IBL). The outer layers have pixel with an area of $50 \cdot 400\mu\mathrm{m}$.

Around the Pixel detector the Semi-Conduct Tracker (SCT) is wrapped. Same as the Pixel detector it is made of silicon, but arranged in stripes rather than in pixels. This allows to cover a wider area. $60\,\mathrm{m}^2$ of silicon are distributed over four barrel layers and two end-caps with nine layers each. In

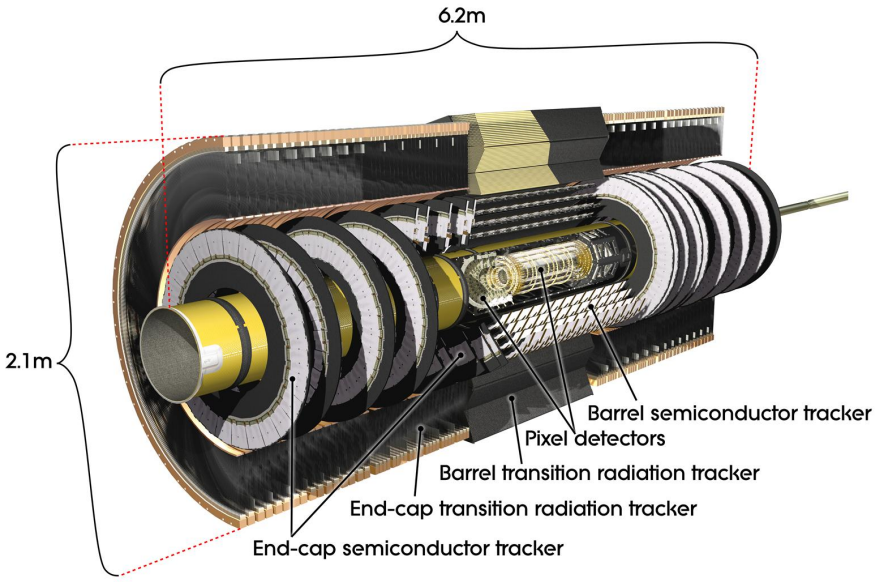

Figure 8: Inner detector. Taken from [4]

the detector readout-strips are placed every 80 µm what allows determining the position of charged particles with an accuracy of 17 µm per layer in the direction transverse to the strips. The detector covers an area of $|\eta| < 2.47$, so charged particles with greater pseudorapidity cannot be detected here.

The last detector in the inner detector is the transition radiation tracker (TRT). The TRT consists of cylindrical drift tubes with conductive coating, also called straws. The straws are filled with a gas mixture based on xenon and in the center of each straw a sense wire is placed. When a charged particles passes a straw it will ionize the gas and as the straws are kept at high negative voltages negative ions will be driven to the sense wire and detected. In between the layers of straws radiators with different refractive indices are used to produce transition radiation. The detector provides drift-time measurements and two independent thresholds. These thresholds allow the detector to differentiate between tracking hits and transition-radiation hits what provides additional information on the particle type.

The whole inner detector is wrapped by central solenoids which provide the inner detector with a magnetic field of about 2 T.

The energy loss of particles before they reach the calorimeter depends on the material they pass before. Therefore a lightweight and uniform material distribution in the inner detector is desired. As this goal cannot be fully reached it is of interest to take a look at the material distribution in dependence on the pseudorapidity (fig. 9). The distribution in dependence on the azimuthal angle is not of great interest as the detector is rather symmetrical.

Calorimeters The information about the calorimeters is taken from [5, 2].

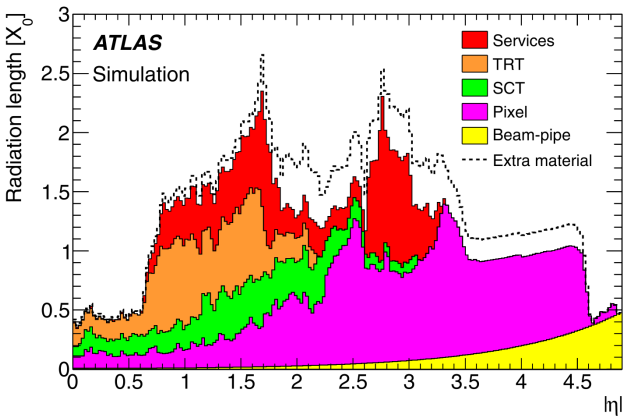

Figure 9: Material distribution of the inner detector. The amount is shown in units of the electron radiation length in dependence on the pseudorapidity η. Graphic taken from [1].

The main goal of the calorimeters is to absorb as many particles as possible by forcing them to loose their energy in the detector. The ATLAS detector contains two calorimeters that cover a range of $|\eta| < 4.9$ and are both built as sampling calorimeters with an active and a passive material. Sampling calorimeters are usually an acceptable compromise between accuracy in the measurements and cost and can be used to cover wider areas.

The electromagnetic calorimeter (EMCal) consists of a barrel part and two end-caps that are divided into smaller parts and it has a fine granularity allowing precise energy measurements. The active medium of the EMCal is liquid argon and lead is used as the passive absorber material, both are arrange in a accordion-shaped structure to provide full coverage in the azimuthal angle. The purpose of the EMCal are energy measurements and identification of particles that interact via the electromagnetic force, for example electrons or photons. In the absorbing material electro-magnetic showers are created that can be detected in the active material.

The hadronic calorimeters (HCal) are build to measure hadronic showers that pass the EMCal due to the strong interaction of hadrons. For $|\eta| < 1.7$ the barrel and the extended barrel tile calorimeters use the iron scintillator-tile technique: Iron as a passive absorber and scintillator tiles for detection. Larger pseudorapidity is covered by the hadronic end-cap and the high density forward calorimeter, both are liquid argon calorimeters and also provide measurements of electromagnetic energy. To reduce hadrons disturbing the muon detector the HCal is much larger than the EMCal with a thickness of 11 interaction lengths at $|\eta| = 0$. In comparison to the EMCal the resolution of the HCal is reduced.

Muon Spectrometer The muon detector consists of muon chambers that use four different types of detecting chambers: The thin gap chamber, the resistive plate chamber, monitored drift tubes and cathode strip chambers. The track of muons can be measured in these chambers and in combination with the toroid magnet system the momentum of muons can be measured precisely.

1.7 Particle Identification

All detector parts are designed for a specific purpose and knowing the signal of the different particles gives us the possibility to reconstruct the events that might have taken place. In table 1 the different particles are listed, together with the detector parts that can be used for their identification. This is going to be used during the event selection and identification in the later Atlantis-part, see section 2.

Particle Type	Inner Detector	EMCal	HCal	Muon Detector
e	✓	✓		
γ		✓		
μ				✓
charged hadron	✓	✓	✓	
neutral hadron			✓	
ν				

Table 1: Particles and the detector part in which they can be identified, so the parts in which they mainly loose their energy.

Electrons will leave a trace in the inner detector and create a shower in the EMCal. Charged hadrons will also create a shower in the EMCal and the shape of the showers has to be used to differentiate electrons and charged hadrons. Photons leave the same trace in the EMCal, but do not leave a trace in the inner detector so they can be distinguished from electrons. Particles that reach the muon detector are most probably muons but a signal in the muon detector might also originate from background or cosmic radiation so a signal in the muon detector needs to be reconstructed to its origin to be sure.

Neutrinos are the only particles we know that leave the detector without interaction. The only chance to detect neutrinos indirectly is to detect missing energy. Furthermore we can only reconstruct the energy balance in the transverse plane, hence reconstruction of the missing energy is also just possible in this plane. The contribution to the missing energy can be written as

$$\begin{aligned} E_x^{\text{miss}} &= -\sum E_i \sin\theta_i \cos\phi_i \\ E_y^{\text{miss}} &= -\sum E_i \sin\theta_i \sin\phi_i \\ E_{\text{t}}^{\text{miss}} &= \sqrt{(E_x^{\text{miss}})^2 + (E_y^{\text{miss}})^2}. \end{aligned}$$

The measurement of the missing energy is rather imprecise, as it depends on all the single contributions that have been measured and therefore carries all the uncertainties. Moreover if more than one neutrino contribute the transverse energy depends on the angle between the two neutrinos.

2 Atlantis

The first part of the experiment was performed with help of the Atlantis-Event-Generator. Six different events were given and the goal was to identify decay products and find a possible process for the observation. Furthermore kinematic variables of the shown products could be read out, these were later used to check whether the stated process is actually possible with regard to conservation laws. Additionally different energy cuts could be applied to adjust the event display to the interesting things and erase the background.

To reconstruct masses the root function `TLorenzVector` was used. This function takes the measured transverse momentum, the angle ϕ and the pseudorapidity η as well as the mass of the observed particle and creates a four-vector out of these informations. Using this four-vector it is possible to determine the invariant mass.

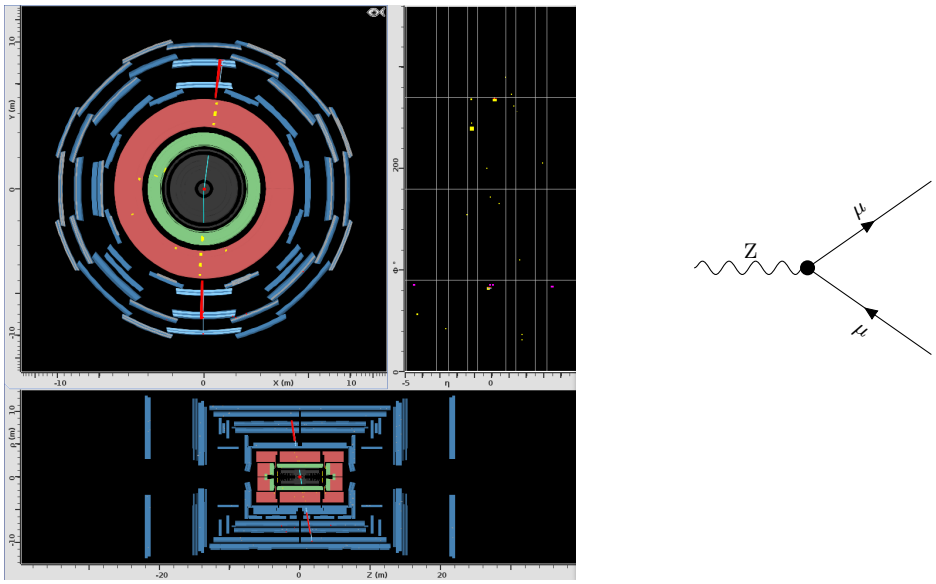

Figure 10: Event display and Feynman diagram for the first event.

Event 1: $\mathbf{Z \to \mu^+\mu^-}$ In the first event two muons were observed, identified by the tracks in the muon-detector that other charged particles do not reach. A possible assumption is that the two muons are the decay products of a Z-boson. This can be checked by calculating the mass of the two muons by adding the two four-vectors and then calculating their norm, which was done with help of the root-function `TLorentzVector`. The result of this computation is 90.55 GeV which is close to $m_Z = 91.1876\,\text{GeV}$, hence justifying the assumption.

Event 2: $\mathbf{W \to \mu\nu\gamma}$ In the second event a muon was observed in the muon detector and some missing transversal energy was found what indicates the existence of neutrinos. Furthermore a photon was detected. Our guess for the decay is, that the mother particle is a W-boson and that

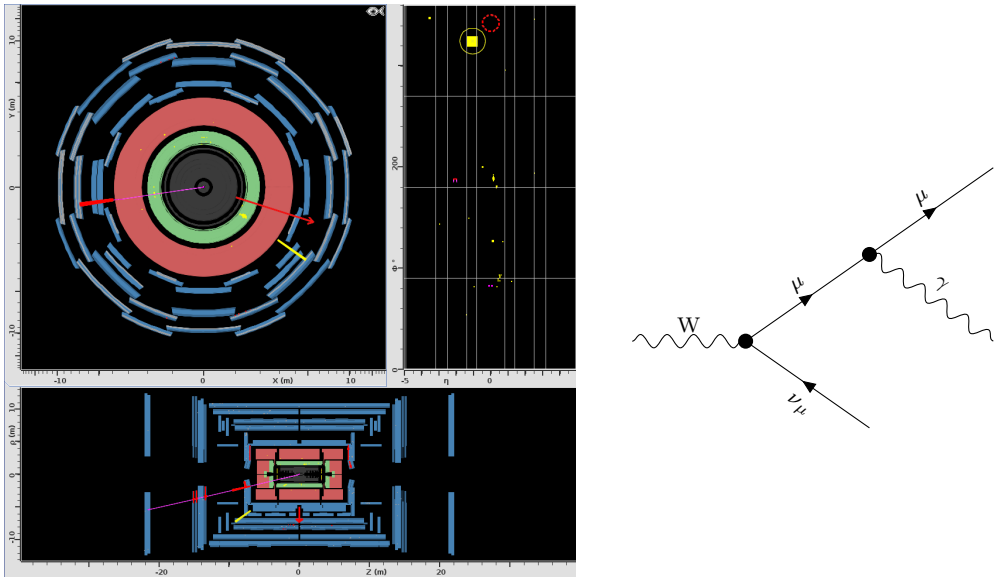

Figure 11: Event display and Feynman diagram for the second event.

the photon comes from bremsstrahlung, so energy loss of the muon in the material of the detector. To check this it would be nice to again calculate the mass of the mother particle, but due to the neutrino this is not completely possible. Due to lepton-number conservation we can state that the missing transverse energy originates from only one neutrino, so at least the transverse mass of the mother particle can be calculated. This has been done with eq. (3) and yields $m_{\mathrm{T}} = 72.35\,\mathrm{GeV}$. This result is smaller than the actual mass of the W-boson $m_{\mathrm{W}} = 80.379\,\mathrm{GeV}$, which is totally fine since we just calculated the transverse mass. Also the energy of the photon is neglected which should also add up to the energy of the mother particle.

Event 3: $\mathbf{t\bar{t} \to b\bar{b}\,\mu^+\mu^-\nu\bar{\nu}}$ In the third event two bottom quarks, two muons and two muon neutrinos are assumed. Of course only the quarks and the muons are detected. A reconstruction of the top-quark mass is not possible, since the neutrinos are not measured individually, but only their summed missing transverse energy is known. Furthermore other than the measured particles, none of the other expected reacting particles needs to be a real particle. Hence, the W-bosons and the top-quarks do not need to be on mass-shell, so they might only contribute as virtual particles. For virtual particles no sensible calculations are possible, although one could still try to estimate some things, since the probability is higher for virtual particles to "occur"/contribute if they are close to on-shell. Nevertheless the invariant mass of the different combinations of muons and bottoms was calculated and we found that one combination (muon down right and bottom top left) leads to a top mass of $m_{\mathrm{mother}} = 323\,\mathrm{GeV}$, so this combination is not possible and these specific bottom and muon have not originated from the same top quark. Hence the other possible combination has been checked and we found $m_{\mathrm{top},\,1} = 102\,\mathrm{GeV}$ for the combination of the bottom right muon and the upper right bottom quark and $m\mathrm{top},\,2 = 125\,\mathrm{GeV}$ for the combination of the bottom left muon and the upper left bottom quark. Therefore these combinations could originate from two top

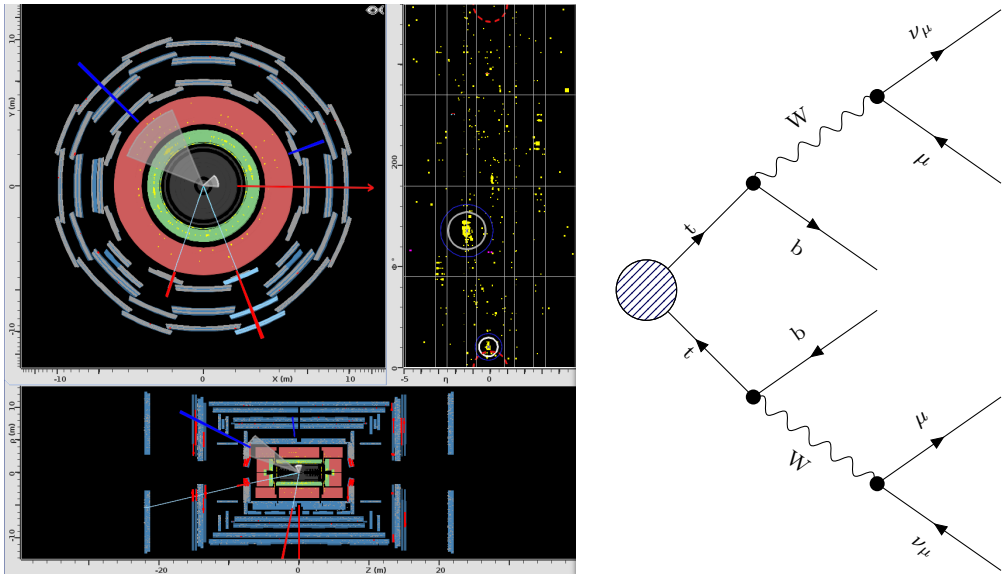

Figure 12: Event display and Feynman diagram for the third event.

quarks and the found mass is lower than the real mass of the top quark, but this makes sense as we do have missing energy from the neutrinos. Thus the calculated masses have to be understood in sense of a lower boundary.

Event 4: $\mathbf{t\bar{t} \to bbe^+e^-\nu\bar{\nu}}$ In the fourth event two bottom quarks, two electrons and two electron neutrinos are assumed. Only the quarks, the electrons and the missing transverse energy are detected/reconstructed by the detector. Just as in the third decay no direct kinematic reconstruction of any particle mass is possible/sensible. Anyway, same as for the previous decay possible combinations can be calculated to determine whether they might originate in two top quark. Combining the bottom quark on the right and electron on the bottom left an invariant mass of the mother particle of $m_{\text{mother}} = 232\,\text{GeV}$ can be calculated, so this combination does not correspond to a top quark. Combining the bottom quark on the left and the electron on the bottom left yields $m_{\text{top, 1}} = 88\,\text{GeV}$ and the other two, the quark on the right and the electron on the upper right give $m_{\text{top, 2}} = 106\,\text{GeV}$ so these can originate from two top quarks. Again the calculated mass is a lower boundary as we did not take the missing transverse energy from the neutrinos into account.

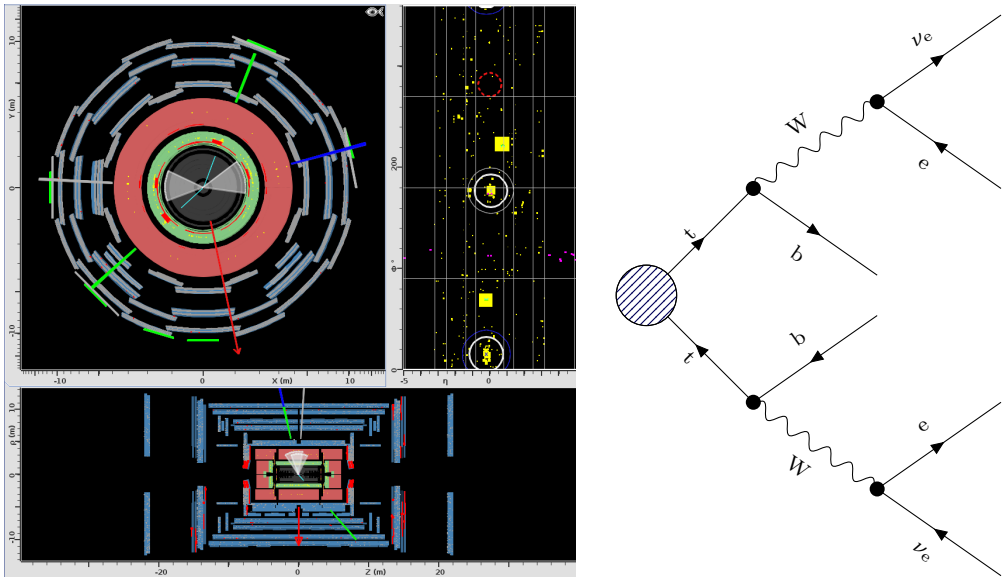

Figure 13: Event display and Feynman diagram for the fourth event.

Event 5: $\mathbf{H \to ZZ \to \mu^+\mu^-\mu^+\mu^-}$ In the fifth event four muons were found in the final state, which indicates a four lepton decay, which is one of the possible Higgs-decay channels. As this decay worked without any missing energy there are no neutrinos and the energy of the mother particle can be directly reconstructed by adding the four four-vector and calculating the norm. This gave us a mass of 120.72 GeV which already is quite close to the mass of the Higgs $m_H = 125\,\text{GeV}$. To further calculate with this process one could also check the masses of the two Z-bosons and find out if we find a combination that leads to one real and one virtual Z. Calculating invariant masses for different combinations of the found muons gives the possibility for $m_{\text{Z1}} = 90.47\,\text{GeV}$ and $m_{\text{Z2}} = 13.73\,\text{GeV}$.

Event 6: $\mathbf{H \to ZZ \to e^+e^-\mu^+\mu^-}$ Again a four lepton process was found but this time with two muons and two electrons. Anyway this still can be a possible decay for the Higgs boson in a process over two Z-bosons. Same as for the last one the invariant mass can be calculated and we got 124.46 GeV. Again this is really close to the current literature value of the Higgs-mass, which justifies the assumed process. Calculating the masses of the Z-bosons for the two electrons and the two muons gives $m_{\text{Z, ee}} = 28.72\,\text{GeV}$ and $m_{\text{Z, }\mu\mu} = 87.53\,\text{GeV}$.

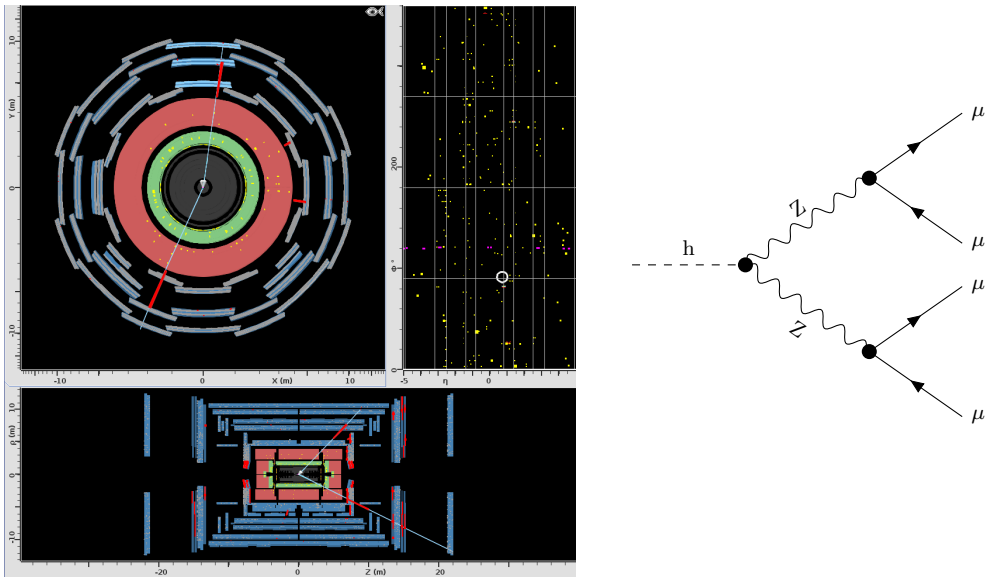

Figure 14: Event display and Feynman diagram for the fifth event.

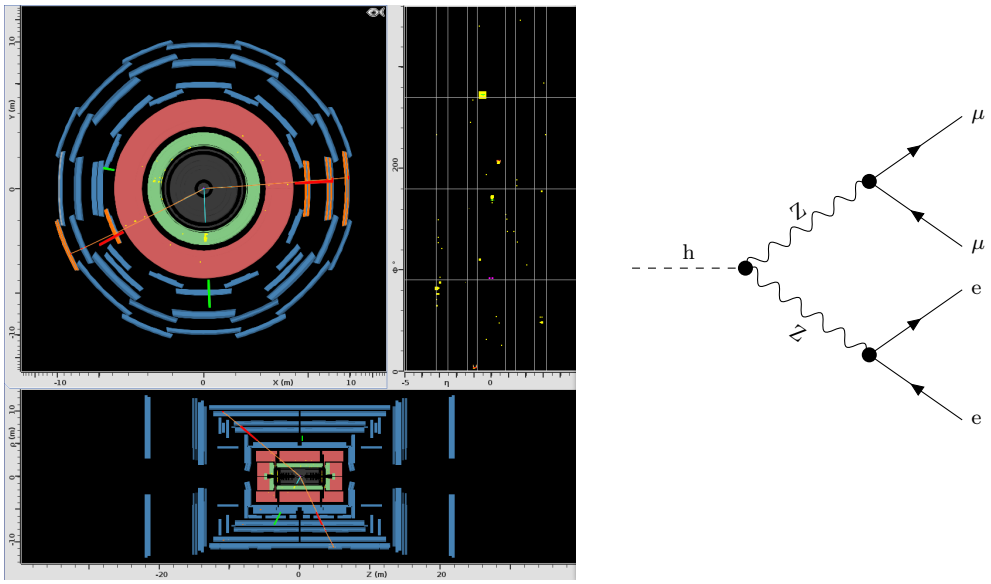

Figure 15: Event display and Feynman diagram for the sixth event.

3 Calorimeter Calibration

To be able to perform useful measurements of the W-boson mass the response of the ATLAS calorimeter has to be precise in its energy measurements. As the material is not distributed equally in the detector, the response of the calorimeter differs in dependence on the region. This difference can be compensated by a calibration that is performed with help of the decay of a Z-boson in an electron-electron pair, $Z \to ee$. The mass of the Z-boson has been measured at LEP with high precision and the process has a large cross-section, so it can be measured in the ATLAS-detector and a calibration in terms of the parameter α can be calculated by

$$\alpha = \frac{E_{\text{meas.}}}{E_{\text{true}}} - 1. \tag{19}$$

$E_{\text{meas.}}$ is determined by fitting a non-relativistic Breit-Wigner function

$$f(M_{ee}) = \frac{\Gamma_Z^2/4}{(M_{ee}^2 - M_Z^2)^2 + \Gamma_Z^2/4}$$

to the invariant mass m_{ee} that is measured in the ATLAS-detector.

3.1 Event Selection

The dataset that is used to determine the invariant mass m_{ee} contains all events with at least one electron with $p_T > 25\,\text{GeV}$. Thus the searched $Z \to ee$-decay is included, but also other events that might fulfill these conditions. The goal of the event selection is to cut the given data by applying reasonable conditions to select all $Z \to ee$-events while the background by other events is cut off without cutting to much of the desired data by too strict rules.

The cuts that were applied, select events that have exactly two electrons with opposing charge, that both fulfill the tightness criteria. Before applying any cuts it was taken a look at different distributions, here we will take a look at the energy of the electrons as an example.

In fig. 16 one can see, that before any cuts the energies of the two electrons differ a lot. Adding to that there is a larger number of electrons that are measured having zero energy (not displayed in the figure because one would not see anything else in that case). This suggests the assumption, that some events with only one electron are measured and stored in the data, therefore the events were cut by selecting events with two electrons. Apart from that two other cuts were implemented. As the searched decay is $Z \to ee$ and the Z-boson is not charged we are looking for a non-charged final state. Hence a cut for opposing electrons was added. This cut did not change the data in a noticeable way, nevertheless it was kept, as it physically makes sense. The last cut asks for the tightness of the two electrons and only events that passed the tightness criteria in both electrons were selected. This cut was implemented to ensure that no fake-electrons contaminate the data.

On the right side in fig. 16 the energy distribution after the three cuts is shown and one can see, that the distributions for the two electrons have converged.

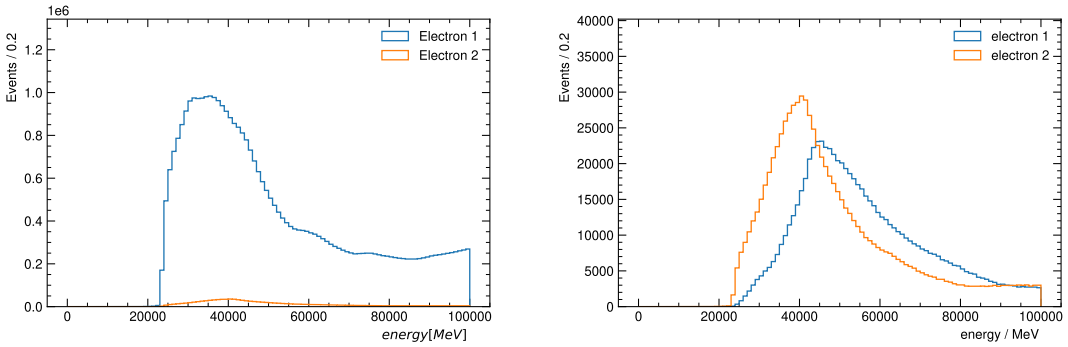

(a) Energy of the electrons before applying any cuts.

(b) Energy of the electrons after applying all cuts.

Figure 16: Change in the energy distribution due to the applied selection rules.

3.2 Invariant Mass for Different Pseudorapidity

The selected events can now be used to determine the invariant mass m_{ee} and calculate the calibration parameter for suitable dependencies. The invariant mass is calculated with help of the two four-vectors of the two electrons, by adding them up and calculating the norm. The four-vectors can be written in dependence of η, ϕ and the transverse momentum p_{T}, were η and ϕ are measured and the transverse momentum can be calculated via

$$p_{\mathrm{T}} \approx \frac{E}{\cosh \eta},$$

as shown in appendix A.1.

The strongest fluctuation in the response of the calorimeter can be seen in the pseudorapidity η, this is due to the high differences in used material as seen in fig. 9. To determine the calibration parameter α in dependence on η the invariant mass has to be determined for different η and plugged into eq. (19). For a sensitive calibration a suitable binning for η has to be chosen.

In fig. 17a the dependence of the events on η is shown. First we note, that the distribution looks comparable for both electrons after the cuts have been applied, which was not the case before. Furthermore we see that evens with an absolute pseudorapidity around zero are more probable. This was expected as in the decay process we analyse forward- or backwards-scattering what would lead to larger η is suppressed. Apart from that we note that for $\eta \approx 1.5$ there have not been any detected events. Taking a look at [5] we find that at $\eta \approx 1.5$ the Barrel-End-caps of the calorimeter form the so called "crack", where no data can be collected.

Now the goal is to find a binning for η that leads to a fine resolution but still has sufficiently high counts in each bin. Adding to that it is desired, that the crack fills an own bin and does not contaminate other bins. We have chosen 15 equidistant bins in a range from $\eta = 0$ to $\eta = 2.47$ and this binning was used to determine the invariant mass for each bin.

In fig. 17b a histogram for the invariant mass for each bin is shown. During the analysis this plot was used and checked for different binnings, until a binning was found which does not show a too high fluctuation between neighboured bins.

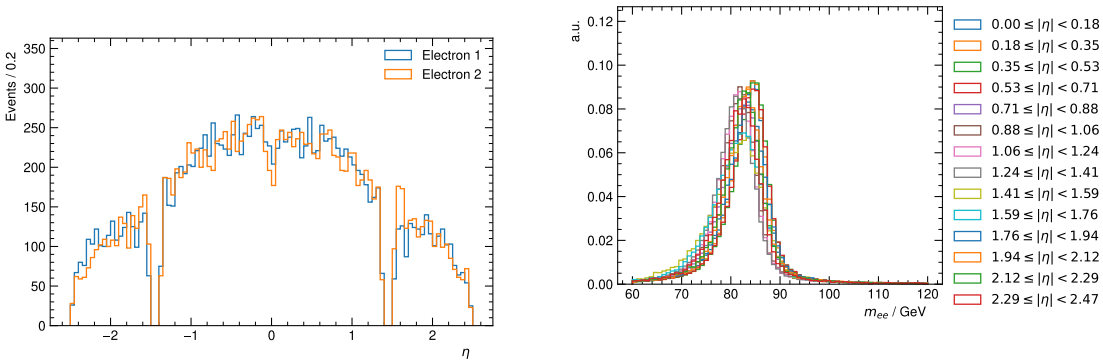

(a) Events in dependence on η after applying the cuts.

(b) Invariant mass for different η bins.

Figure 17: Pseudorapidity η and the invariant mass for different bins.

3.3 Calibration

For this fixed binning in η for each bin a Breit-Wigner fit is performed and the invariant mass is calculated. According to the mass found in the fit the calibration parameter α was calculated. The calculated parameter for all bins is shown in fig. 18. For all η the calibration is of the same magnitude and one can see a small dip in calibration around the crack, this is sensitive as this is a region with more fluctuation in material than the extrema.

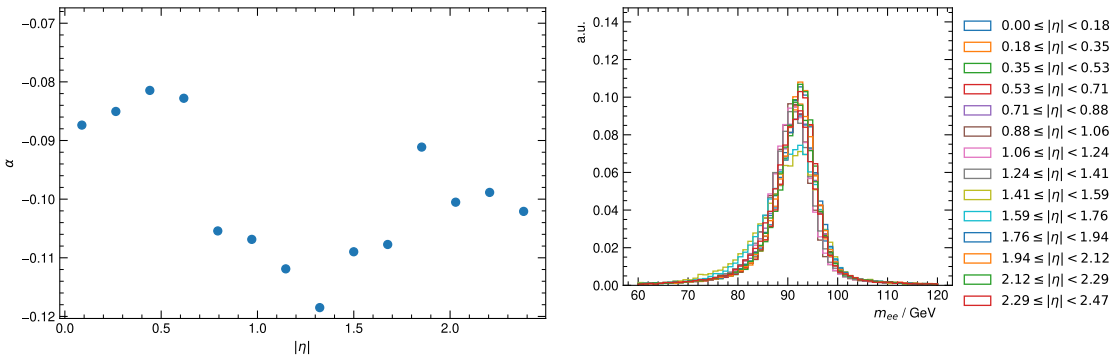

(a) Calibration parameter alpha for each bin.

(b) Invariant mass for η bins after calibration.

Figure 18: Calibration parameter and result of applying the calibration.

This calibration can now be applied on the data to check the invariant mass again. This was done for each bin and the plot is shown in fig. 18. The plot gives a good insight that the calibration was rather successful, as all bins now behave the same way. The only two lines that are significantly lower than the other belong to the two bins containing the crack, so also this behaviour is expected. Furthermore the calibrated data was fitted for every bin and the invariant mass was calculated by

taking the mean over all bins and using the standard deviation as an error:

$$m_{ee} = (90.7 \pm 0.6)\,\mathrm{GeV}.$$

4 W-Boson Mass

The goal of this part of the experiment is to determine the mass of the W-boson. As the precision of the measurement is limited by the decay products a suitable decay channel has to be chosen. On the one hand a process with a rather hight cross-section is desired, on the other hand a process with precisely measurable decay products is needed. The decay of the W-boson to hadronic jets has a rather large branching ratio, but the measurement of these jets does not yield as good results as the measurement of leptons. This is due to the better resolution of the electro-magnetic calorimeter in comparison with the hadronic calorimeter and therefore the decay $W \rightarrow l\nu$ is going to be analysed.

4.1 Data and Monte Carlo Samples

The given data does again not only contain the interesting events, but every event with at least one lepton with transverse momentum $p_T > 25\,\text{GeV}$. Thus the data needs to be cutted so only the relevant events add to the measurement. This data selection is done with help of simulated Monte Carlo data for all decays that may occur and the goal is to achieve a good agreement in different kinematic variables.

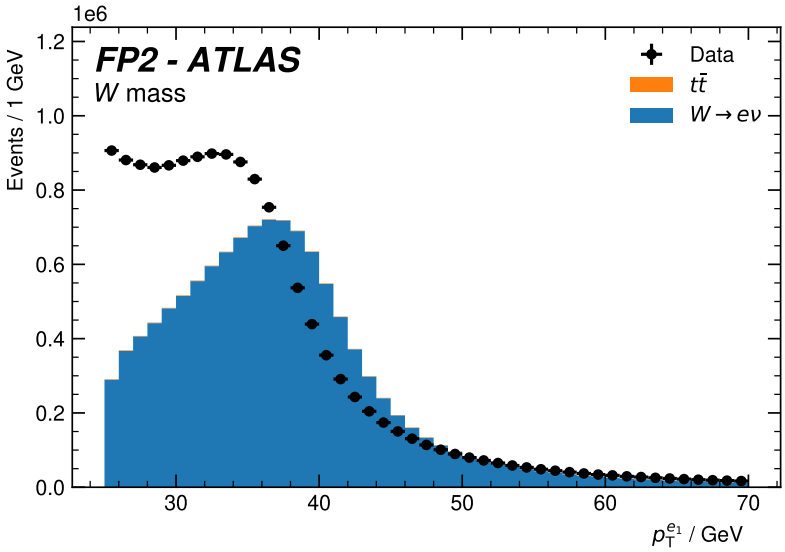

Figure 19: Transverse momentum of the first electron before any major cuts have been applied.

In fig. 19 the agreement between data and Monte Carlo data is shown before any major cuts have been applied. One can clearly see, that there is a huge difference and that it might not be enough to add more background processes to the Monte-Carlo data. First we notice, that the data is shifted towards the MC-data, this is due to the missing calibration that has not been applied yet. But even if the data was shifted a little the agreement would be sobering. This difference between data

and MC is due to the existence of so called "fakes". The preselected data we get from the detector only takes events that have on lepton with a minimal transverse momentum. This is useful for us, as the amount of data we would get otherwise would be overwhelming but has the disadvantage that the detector might be wrong in its decisions. Therefore some events are selected as an event with at least one lepton that do not contain a lepton, but a really lepton-like jet. This problem can be solved by determining the amount of fakes out of the data, thus two different selection processes are implemented, one for fakes and one for the rest of the data. The first two cuts that have been made apply to both types of events: Every event that is considered has to have exactly one lepton (or at least the detector should tell us that it has one) and there should be missing transverse energy $MET > 20\,\text{GeV}$. Both cuts make sense and are mandatory (event though the amount of missing transverse energy can be discussed), as were are looking for the W $\rightarrow$ lν decay, so we have one lepton in the end and a neutrino that will be detected as missing energy. The obtained histograms after these two cuts are shown in fig. 20.

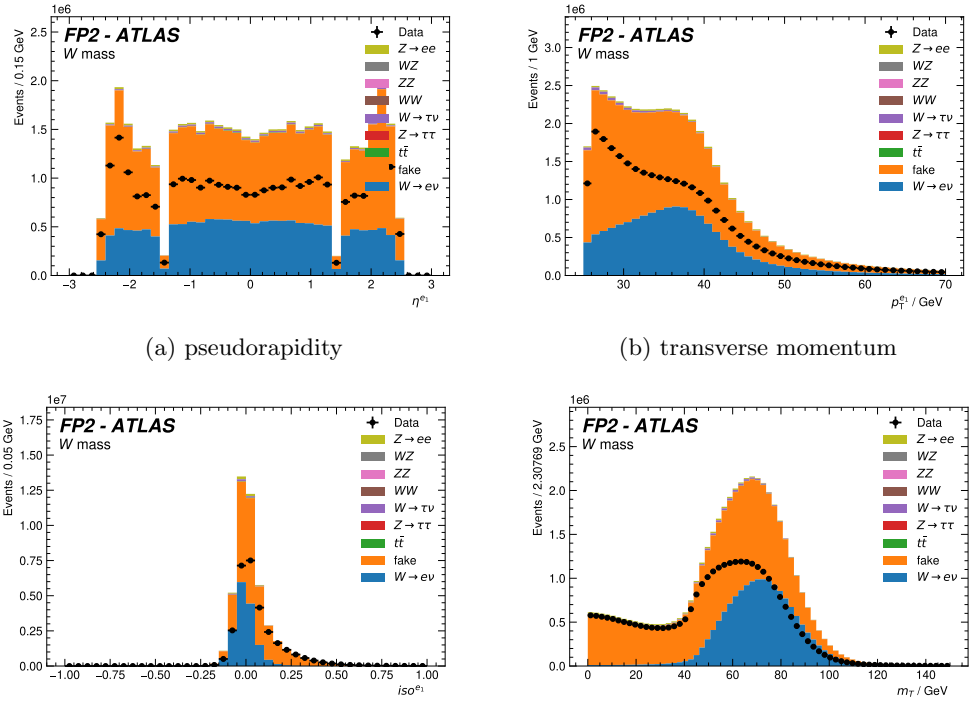

(a) pseudorapidity

(b) transverse momentum

(c) isolation parameter

(d) transverse mass

Figure 20: Different kinematic variables after the general cuts were applied.

Taking a look at the histograms we clearly see that more cuts need to be applied and that there is a need to differentiate between fakes and true data. The two parameters that seemed the most sensitive to take a look are isolation and tightness. An event that is considered a fake should be good enough to pass the general cuts, otherwise it would not be a fake event but just a not-interesting event, but it should be too bad to pass the strict selection criteria. To get a feeling for

both parameters the same kinematic variables as before were taken a look at. Each time with the general cuts applied, once with cuts in terms of tightness (see fig. 22) and once with help of the isolation parameter (see fig. 21).

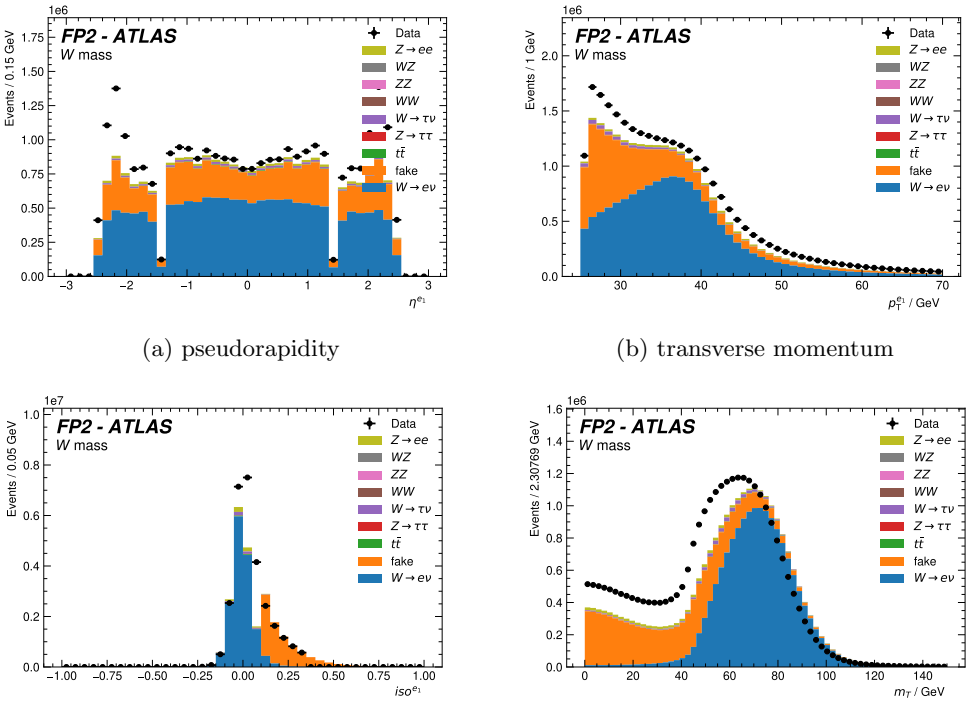

(a) pseudorapidity

(b) transverse momentum

(c) isolation parameter

(d) transverse mass

Figure 21: Different kinematic variables for the general cuts and a selection with regard to the isolation parameter $\mathfrak{I}$. For fake events $\mathfrak{I}_{\text{fake}} > 0.1$ has to apply and for non-fakes $\mathfrak{I}_{\text{n.f.}} < 0.35$ was set.

In fig. 21c we can see, that the selection of the fakes lead to the expected result and cut all fakes with isolation around zero, bringing the data closer to the Monte Carlo data. Also the other kinematic variables show a closer relation between data and Monte Carlo data.

The second criteria that was chosen is the tightness of the electron. Tightness in this context means, that there are different criteria and a real lepton will pass this strict selection rule and carry a $\mathfrak{T}$ == `True`, while a false lepton, so for example a quark-jet does not pass this criterion. Hence, this can be applied to select fakes that were good enough to pass the general selection, but are not the events that we are actually interested in. In fig. 22 different kinematic variables with the general cuts and the tightness selection applied are shown. Same as for the variables after applying the isolation selection, we see that the data and the Monte Carlo data got closer, but comparing fig. 21 and fig. 22 we see that both cuts show an absolute difference between data and Monte Carlo data, but in different directions. Thus the insight in these two selection criteria was used to try a combination of both, in hope that the over- and underestimation combine and cancel

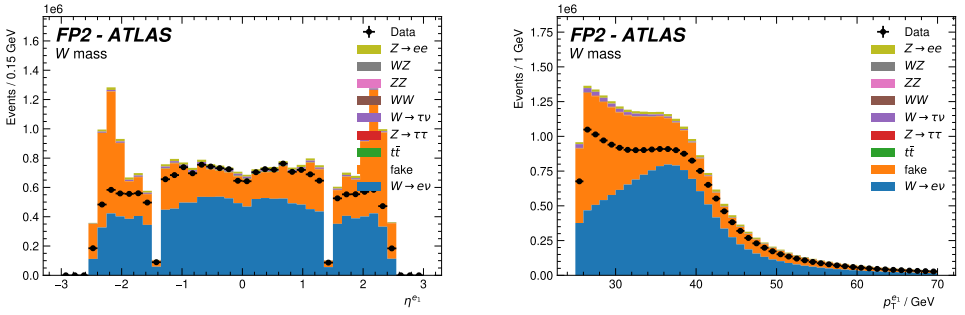

(a) pseudorapidity

(b) transverse momentum

(c) isolation parameter

(d) transverse mass

Figure 22: Different kinematic variables for the general cuts and a selection with regard to the tightness $\mathfrak{T}$. For fake events $\mathfrak{T}$ == `False` was expected and the non-fakes should satisfy $\mathfrak{T}$ == `True`.

out.

In fig. 23 the kinematic variables with the final cuts applied are shown. For most of the variables the data lies nicely on the Monte Carlo data, nevertheless there still is some discrepancy. It was tried to find better combinations of the mentioned parameters but the settings mentioned above are the best that were found. Also it has to be mentioned, that the whole selection process is limited by comparing the fit of data and Monte Carlo by eye.

4.2 Reweighing the Monte Carlo Samples

Later we are going to determine the mass of the W-boson by comparing our measured transverse momentum to the solution of different mass hypothesis. Thus we need simulated Monte Carlo data for all hypothesis we are going to test. Since the generation of this data is computationally heavy just generating this data can not be done in a reasonable amount of time. Therefore the existing data is used and shifted to different mass hypothesis, the data is reweighed.

In fig. 24a the process is illustrated: For a given distribution (in our case the existing MC-samples for $m_{\mathrm{W}} = 80.4\,\mathrm{GeV}$) the weights needed to go from the old to a new distribution can be calculated

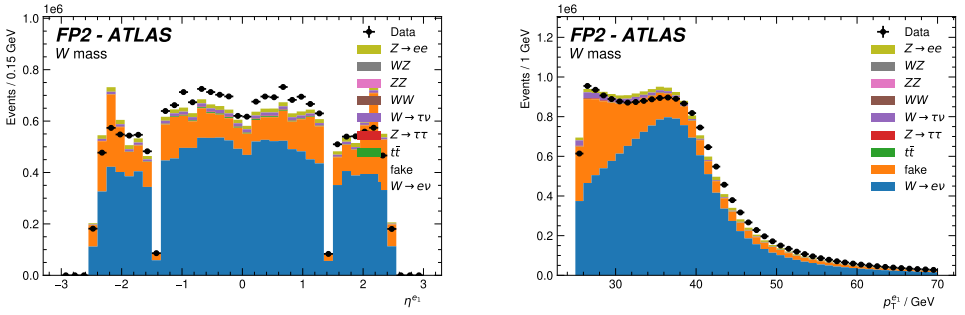

(a) pseudorapidity

(b) transverse momentum

(c) isolation parameter

(d) transverse mass

Figure 23: Different kinematic variables after general cuts, the tightness criterion and the isolation selection as describes before were applied.

via

$$f(x) = \frac{N(x|m_{\text{new}})}{N(x|m_{\text{old}})}$$

and this calculation can also be used to go to a new distribution for known weighting factors. The transverse mass follows a Breit-Wigner distribution. This can be used to determine the weighting factors, by determining the Breit-Wigner function for the given MC-samples with a fit and calculate the weight needed to go from the fitted Breit-Wigner function to one that is shifted to the new mass. The process is illustrated in fig. 24.

The calculated weight-factors can now be used to determine the reweighed distribution of any variable out of the one set of MC-samples we do have, so it is possible to test our data for the transverse momentum of the electron against any weight-hypothesis we might have.

4.3 Statistical Analysis

Now that the data is cut and we can create Monte-Carlo samples for any mass hypothesis we are interested in the mass of the W-boson can be determined by fitting different hypothesis to the data.

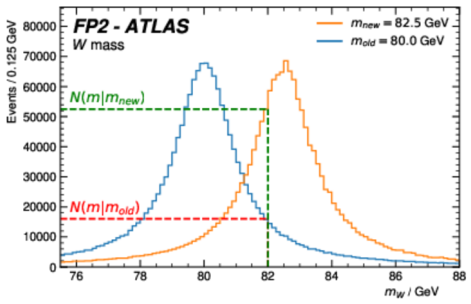

(a) Sketch that shows how the existing data can be reweighed to different mass hypothesis.

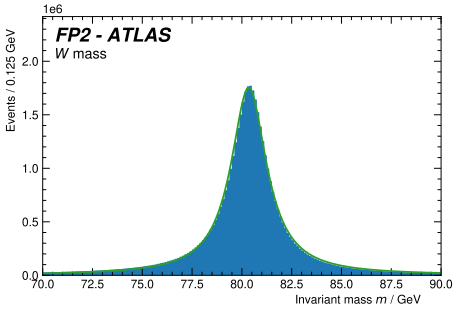

(b) Breit-Wigner fit on the MC-samples.

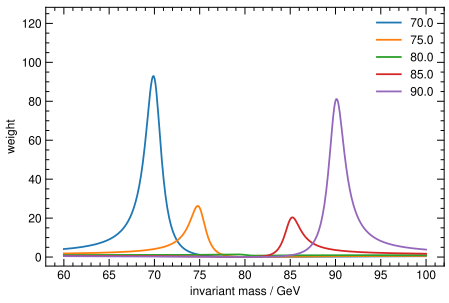

(c) Reweighing parameters for different mass hypothesis.

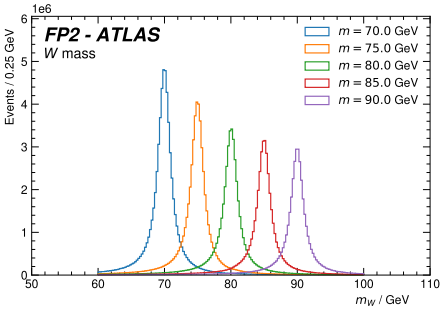

(d) Weighting factors applied on the MC-data.

Figure 24: Precess to reweigh MC-samples. The fitted Breit-Wigner function on the existing data is used to determine the reweighing parameters for different mass hypothesis. The determined weight factors can now be used to shift the MC-samples to the new mass hypothesis.

The hypothesis has two different parameters: The mass of the W-boson and the fake-factor.

In fig. 25 a comparison between hypothesis and data for different fake factors is shown. We see that a larger fake-factor leads to a higher curve for lower transverse momentum, this is expected, as for lower transverse momentum we do expect more fakes due to QCD-effects. A mass change in the hypothesis would lead to a lower curve for lower masses and vice versa.

In the following the best values for these parameters are estimated with help of the negative log-likelihood (NLL) minimisation method. For both, the hypothetic mass and the fake-factor sensitive ranges have to be determined for which the minimum of the NLL is determined. These ranges were found with help of the histograms fig. 25. The found minimum then is the best estimate that is found under the given conditions. Besides giving a possibility to estimate the optimal parameters, the NLL-method can also be used to determine errors on the estimation via

$$-\ln L(\hat{x} \pm n\sigma) = -\ln l(\hat{x}) + \frac{1}{2}n^2,$$

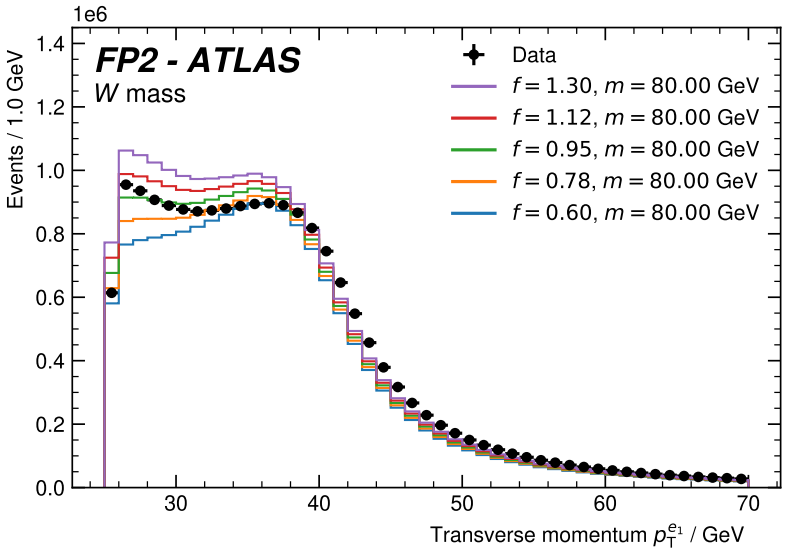

Figure 25: Transverse momentum of the electron as found in the data in comparison to hypothesis with $m_W = 80\,\text{GeV}$ and different fake factors.

where $\hat{x}$ is the best found estimate for the parameter. The estimation of the best parameters together with the error estimation yields

$$m_W = 83.473^{+0.004}_{-0.007}\,\text{GeV},$$
$$f = 1.119^{+0.003}_{-0.002}$$

In fig. 26 the best estimate with its errors and the kinematic variables for these values are shown. For the found parameters the data fits the MC-samples very well, even though there are some discrepancies for all variables.

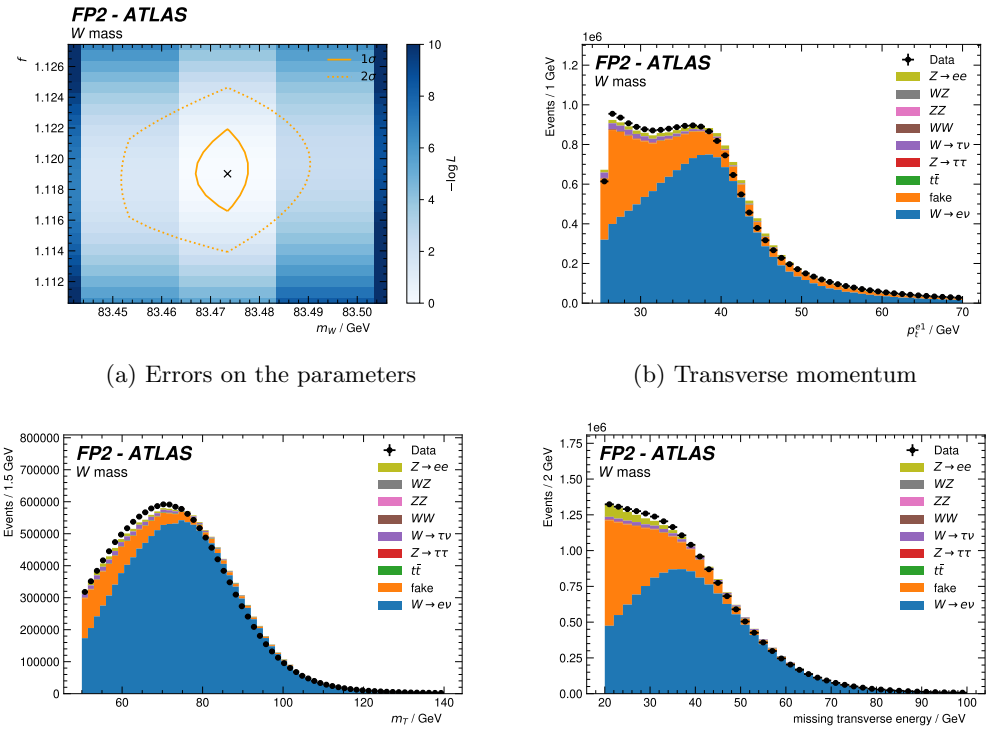

(a) Errors on the parameters

(b) Transverse momentum

(c) Transverse mass

(d) Missing transverse energy

Figure 26: a) Visualisation of the found best estimate for the mass and the fake-factor together with the errors. b), c), d) Different kinematic variables for the best estimates.

5 Higgs Search

In this section we analyze the Run1 dataset at $\sqrt{s} = 8\,\text{TeV}$. This analysis is split into two parts. First we begin in "data-blind"-mode, where we work exclusively on Monte-Carlo simulation data. The main task is to apply cuts to the Monte-Carlo data in a way that the Higgs signal for the four lepton decay is of maximal statistical significance. After the final choice for the cuts is set we "unblind" the data and check if we got a Higgs signal, which allows to discard the "background only"-hypothesis. So we start off describing the "data-blind"-phase.

5.1 "Data-Blind"-Phase

The main indicators for the quality of the chosen cuts are the histograms of the kinematic variables and the significance plots of the signal for the different kinematic variables. The significance plots show the signal significance estimator $s/\sqrt{b}$ for every bin, where s is the number of signal events and b is the number of background events. The estimator indicates how many Poisson standard deviations from the background-only-model the signal corresponds to. Thus the choice of the cuts was an iterative process. We started choosing the isolation parameters until the signal significance was maximal. Afterwards the cuts on the impact parameter significance where chosen, again trying to maximize the signal significance. Then the rest of the cuts where chosen in an iterative manner as explained below. For the sake of readability and clarity the plots, which show the cutting process, are shown in appendix B.

Lepton Number The most obvious cut which was set was that in the final state (the measurement) are exactly 4 leptons, since we are interested in the search channel shown in fig. 5.

$$N(\text{leptons}) = 4$$

Charge Neutrality Since we are interested in leptons, which are originating from an Higgs particle decay, the total charge of the final state needs to be zero, since the Higgs particle is charge neutral.

$$\sum_{i=1}^{4} Q_i = 0$$

Isolation Parameter Here we exclusively orientated us on the significance plot for the m_{4l} histogram. We also chose a harder cut for the electrons since muon events are less likely to be misinterpreted because of the detectors architecture.

$$\begin{aligned} \mathfrak{I}(p_T, \text{electron}) &< 0.4 \\ \mathfrak{I}(E_T, \text{electron}) &< 0.4 \\ \mathfrak{I}(p_T, \text{muon}) &< 0.6 \\ \mathfrak{I}(E_T, \text{muon}) &< 0.6 \end{aligned}$$

The impact of these cuts is displayed in figs. 35, 41 and 42, which are found in the appendix.

Impact Parameter Significance Once again we orientated us on the significance plots. And again we imposed a harder cut to the electron impact parameter significance.

$$IPS(\text{electron}) < 5$$
$$IPS(\text{muon}) < 6$$

The impact of these cuts is displayed in figs. 36, 41 and 42, which are found in the appendix.

Transverse Momentum of Individual Leptons For these cuts we looked at the histograms of the transverse momenta of the individual leptons. We chose our cuts in a way, that we cut off background events, but keeping signal events. Afterwards we checked for the signal significance, which stayed roughly the same. The histograms for the final cuts are shown in fig. 29

$$p_{T,l_1} > 20\,\text{GeV}$$
$$p_{T,l_2} > 12\,\text{GeV}$$
$$p_{T,l_3} > 8\,\text{GeV}$$
$$p_{T,l_4} > 1\,\text{GeV}$$

The impact of these cuts is displayed in figs. 37, 41 and 42, which are found in the appendix.

Invariant Masses m_{12} & m_{34} For this cut the line of reasoning is a bit more physical than the other ones. For a Higgs Boson with $m_\text{H} < 2 \cdot m_\text{W}$ it is clear to see that for the $\text{H} \to \text{W}^-\text{W}^+ \to l\bar{l}l\bar{l}$ channel, not both W bosons can be on-shell because of 4-momentum conservation. Hence we chose the cuts in a way which restricts the more energetic lepton pair to come from a rather close to on-shell W boson, while the less energetic lepton pair can come from a virtual W boson which is rather "below" the mass-shell (Even though, the on-shell mass is included in the mass interval.).

$$50\,\text{GeV} < m_{12} < 110\,\text{GeV}$$
$$10\,\text{GeV} < m_{34} < 110\,\text{GeV}$$

The impact of these cuts is displayed in figs. 38, 41 and 42, which are found in the appendix.

Invariant Mass m_{4l} Finally we chose a cut for the total invariant mass of the measured 4 leptons. This mass window is again justified by the $m_\text{H} < 2 \cdot m_\text{W}$ assumption. Furthermore a lot of background and no signal was visible below 100 GeV.

$$100\,\text{GeV} < m_{4l} < 180\,\text{GeV}$$

These cuts result in the invariant four lepton mass histogram shown in fig. 27a. The signal significance for the MC-simulation data is shown in fig. 27b. At this point we chose to "unblind", even though the significances for the simulated data where below 3σ for all Higgs models. The P-value plot for the simulated data is shown in fig. 28. We then moved on and "unblinded" the data.

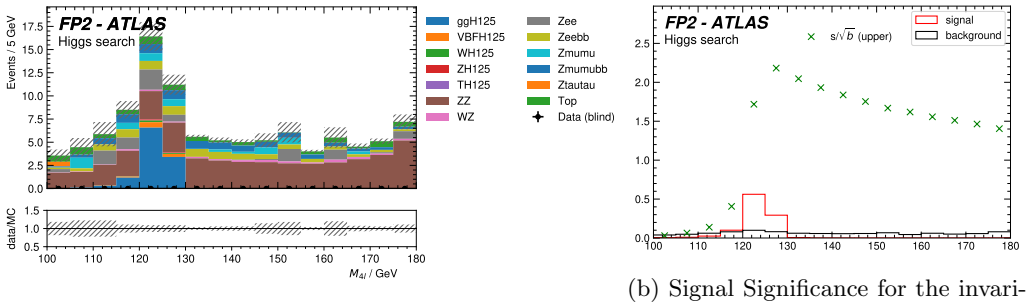

(a) Invariant 4 lepton mass distribution

(b) Signal Significance for the invariant 4 lepton mass distribution

Figure 27: In this figure the distribution of the invariant 4 lepton mass and the associated signal significance is shown.

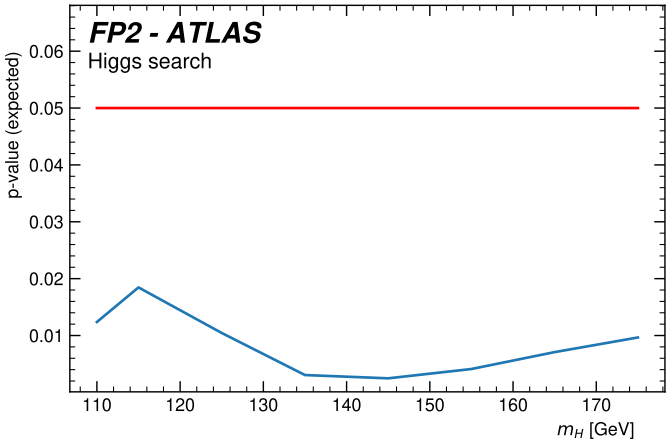

Figure 28: In this picture the p-value plot for different Higgs-mass models using the simulated signal is shown.

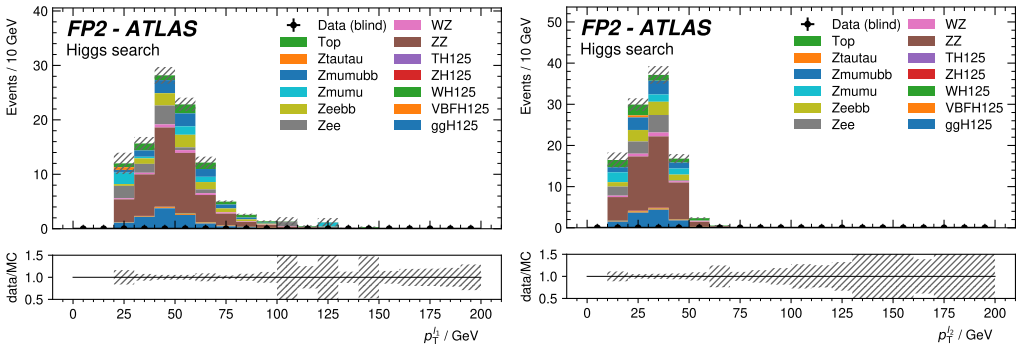

(a) Transverse Momentum of Lepton 1

(b) Transverse Momentum of Lepton 2

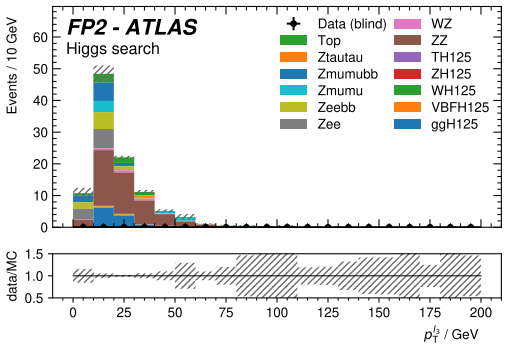

(c) Transverse Momentum of Lepton 3

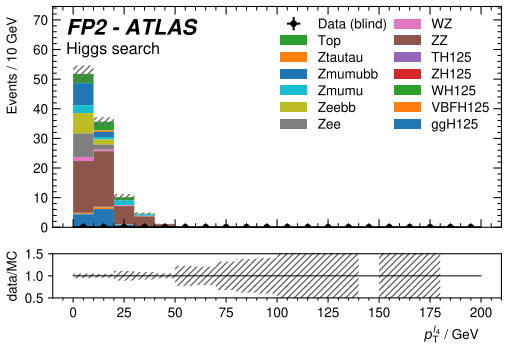

(d) Transverse Momentum of Lepton 4

Figure 29: In this figure the transverse momentum distributions for each individual lepton are shown.

5.2 “Unblinded”-Phase

In this task we basically just compiled the code which was given. At first we examined the histograms for the kinetic observables and checked how good they match the measurements. The histograms including the data is shown in figs. 30 and 31. Even though for some of the points the measured data and the simulation data do not agree within one standard deviation, but the trend seems quite good.[12]

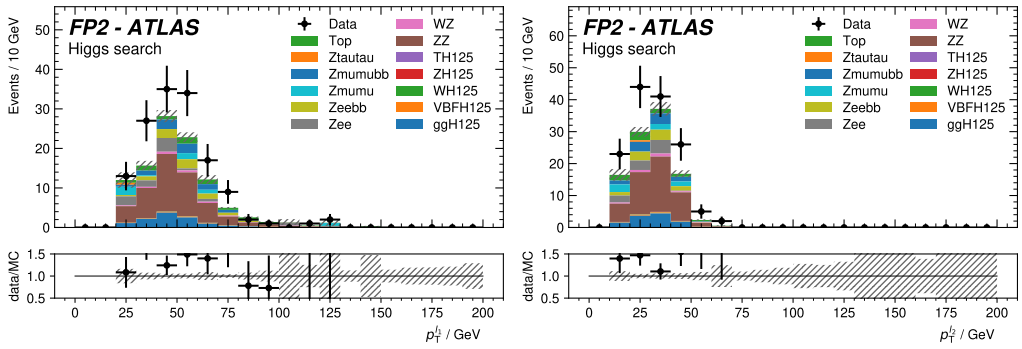

(a) Transverse Momentum of Lepton 1

(b) Transverse Momentum of Lepton 2

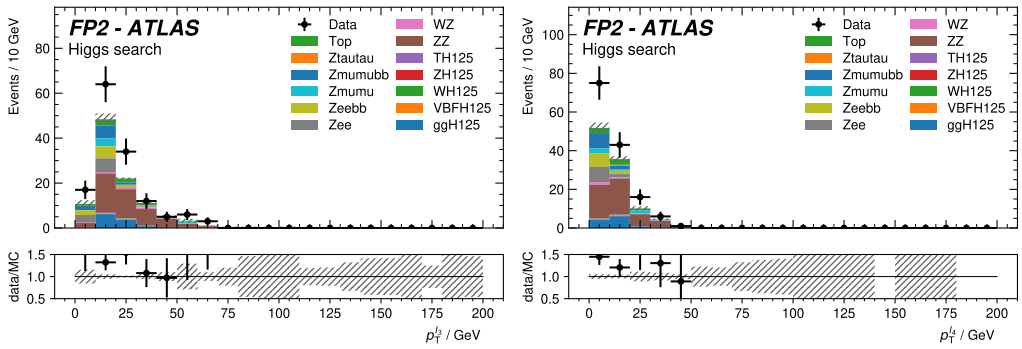

(c) Transverse Momentum of Lepton 3

(d) Transverse Momentum of Lepton 4

Figure 30: In this figure the transverse momentum distributions for each individual lepton are shown.

[12]Since there is not much information given on how many perturbative orders where used in the simulation data and how all the errors where estimated, it is hard to give a reasonable explanation for the deviation (and its magnitude) between simulation and measurement.

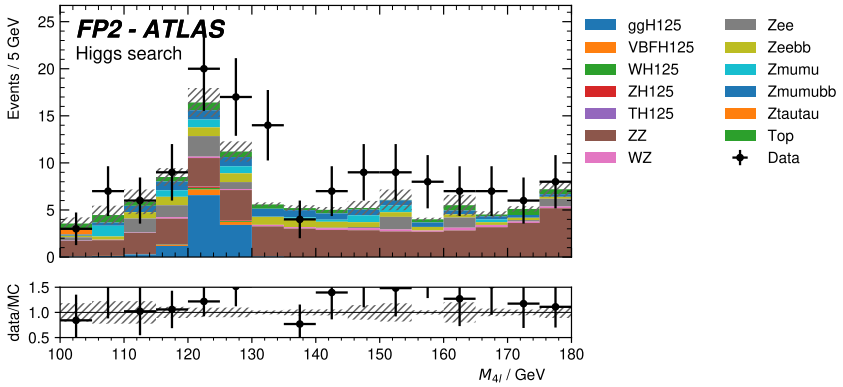

Figure 31: Invariant 4 lepton mass distribution including the measurement data.

P-Values and Fit Now the cutted data is tested against the "$s + b$"-hypothesis for different Higgs-masses, while the initial hypothesis is the background only hypothesis. To discard the initial hypothesis at a significance of 5% we need a p-Value of $p < 0.05$. Furthermore, in physics we speak of a discovery for a significance of $\sigma \geq 5$. The results of the statistical analysis performed by the program, which was given, are listed in table 2. The p-Values are also shown in fig. 32

Table 2: In this table the p-values and significances for the different Higgs-mass hypothesises are listed.

Higgs Mass m_h / GeV	p-Value	Significance / σ
110	0.128	1.18
115	0.004	2.81
125	$4.2 \cdot 10^{-8}$	5.02
135	0.014	2.29
145	0.021	2.06
155	0.022	2.02
165	0.109	1.23
175	0.302	0.50

As seen in table 2 we achieved a $\sigma = 5.02$ signal for the $m_{\mathrm{H}} = 125\,\mathrm{GeV}$ model. Hence, we discovered the Higgs boson. To get an estimate for the Higgs mass, which should be really close to 125 GeV due to the model significance, a fit to the data shown in fig. 31 was performed. The model function which is fitted to the data is given by

$$f(x; A, \mu, \sigma, B, C, D) = A\,\mathrm{e}^{\frac{(x-\mu)^2}{\sigma^2}} + B + C\,x + D\,x^2 \tag{20}$$

The fit results are shown in table 3 and the fit is also plotted in fig. 33. The position parameter μ of the gauss function in the fit model was estimated to be $\mu = (125 \pm 1)\,\mathrm{GeV}$ which is in full accordance with the literature and the model we used for the significance estimation.

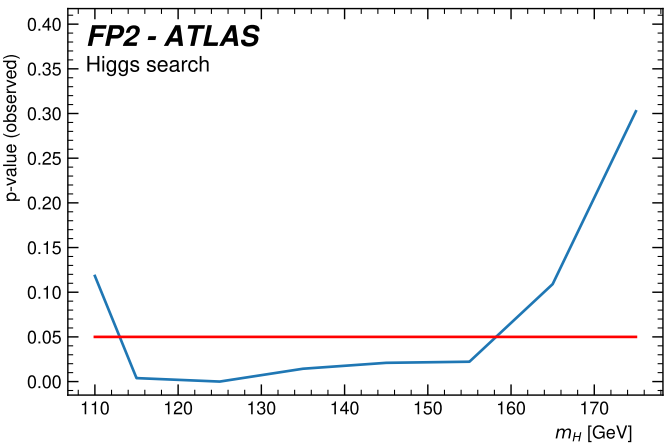

Figure 32: In this picture the p-value plot for different Higgs-mass models against the measured data is shown.

Table 3: In this table the results for the model fit are shown. The model which was used is given in eq. (20) and the plot for the fit and the data are shown in fig. 33

Parameter	Value
A	15 ± 4
μ	$(125 \pm 1)\,\mathrm{GeV}$
σ	$(5 \pm 1)\,\mathrm{GeV}$
B	-15 ± 26
C	0.27 ± 0.40
D	-0.0008 ± 0.0014

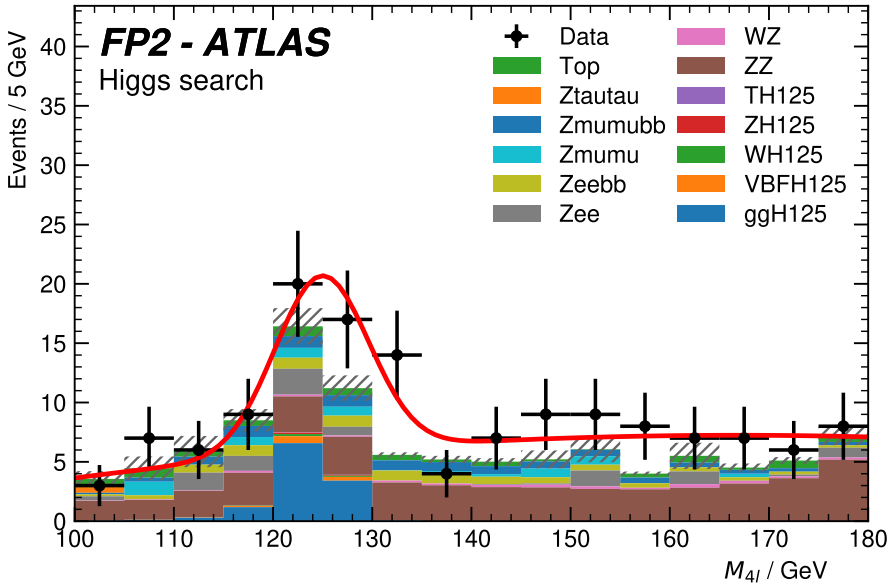

Figure 33: In this figure the results for the model fit are shown. The model which was used is given in eq. (20) and the fit parameters for the fit are shown in fig. 33

6 Summary and Discussion

Atlantis-Event-Generator In the first part of the experiment the Atlantis-Event-Generator was used to analyse different processes with help of their decay products. The determined processes are:

$$\begin{aligned} Z &\to \mu^+\mu^- \\ W &\to \mu\,\nu\,\gamma \\ t\bar{t} &\to b\bar{b}\;\mu^+\mu^-\nu\bar{\nu} \\ t\bar{t} &\to b\bar{b}\;e^+e^-\nu\bar{\nu} \\ H &\to ZZ \to \mu^+\mu^-\mu^+\mu^- \\ H &\to ZZ \to e^+e^-\mu^+\mu^-. \end{aligned}$$

For the processes without neutrinos the invariant mass of the mother particle was calculated to check the assumed decay, for processes involving neutrinos only the transverse mass could be calculated. All calculations gave good indications that the assumed decays are right. The last two decays are possible decays of the Higgs boson and these decay chanels were used later in the search of the Higgs boson.

Calibration of the Calorimeter In the second part of the experiment the calorimeter was calibrated. This was done by determining the mass of the Z boson the ATLAS detector measures witout calibration and comparing to the Z mass measured precisely at LEP. First the ATLAS data was cutted so only the $Z \to ee$ decay was included, afterwards the invariant mass of the Z boson was calculated for different pseudorapidity. This was done by binning the pseudorapidity, therefore also the calibration in the end depends on η, which is a sensitive parameter as the material distribution in the detector fluctuates a lot in dependence on the pseudorapidity. To check the calibration it was applied on the ATLAS data and the mass of the Z boson was calculated as a mean over all bins. This calculation yields

$$m_{ee} = (90.7 \pm 0.6)\,\text{GeV}. \tag{21}$$

This result is close to the mass of the Z boson of $(91.1876 \pm 0.0021)\,\text{GeV}$ as given by the Particle Data Group [10] and this literature value lies in one standard deviation of the calibrated measurement of the ATLAS detector. Therefore it was decided to use the determined calibration in the following parts. Nevertheless a better calibration probably could have been achieved by not only considering the pseudorapidity but performing a two-dimensional calibration that also depends on the transverse momentum of the particles.

W-Boson Mass To determine the mass of the W boson in the thid part of the experiment, the decay of the W boson in a lepton and a neutrino was chosen as a decay chanel. Again the given data was cut to achieve a good selection of the interesting events, this was done with help of simulated Monte-Carlo data. Besides taking background into account a selection for fake events had to be applied. To determine the W mass the selection of data and MC data was tested againdst different mass hypothesis realised by shifting the MC data to different masses. The best fit for the mass and

the fake facor was determine with the Negative-Log-Likelihood method and the error was estimeted by $-\ln L + 1/2$ and the result is

$$m_{\mathrm{W}} = 83.473^{+0.004}_{-0.007}\,\mathrm{GeV},$$
$$f = 1.119^{+0.003}_{-0.002}.$$

This is not compatible with the mass as given by the Particle Data Group of (80.379 ± 0.012) GeV [10]. One reason for the difference of the calculated value and the literature value lies in the calibration of the calorimeter but this was difficult to consider, as the results of the calibration were used without error estimation. Furthermore the event selection might not have been optimal and was only performed by eye which makes it difficult to find the best fit. Adding to that the MC data was only shifted to different mass hypothesis as generating this data for every hypothesis would take too much time, but shifting the data also generated errors that cannot easily be used later.

Higgs Search The last part of the experiment was the search for the Higgs boson. With help of Monte-Carlo data cuts were applied that isolated the chosen four lepton decay chanel while trying to keep a maximal statistical significance. After all cuts were chosen the data was unblinded and the cuts were applied on the data, but not changed anymore. Now the different mass hypothesis were tested againdst the real data and the mass of the Higgs boson was determine as

$$m_{\mathrm{H}} = (125 \pm 1)\,\mathrm{GeV} \tag{22}$$

with a significance of 5.02σ and a p-value of $4.2 \cdot 10^{-8}$. A significance of $\sigma \geq 5$ corresponds to a discovery, so with the set cuts in combination with the given data it was possible to isolate the chosen decay chanel with high precision without loosing too much events.

References

[1] G. Aad et al. "Electron performance measurements with the ATLAS detector using the 2010 LHC proton-proton collision data". *The European Physical Journal C* 72.3 (2012). DOI: 10.1140/epjc/s10052-012-1909-1. URL: http://dx.doi.org/10.1140/epjc/s10052-012-1909-1.

[2] *Atlas Experiment - Discover the Detector*. URL: https://atlas.cern/sites/atlas-public.web.cern.ch/files/inline-images/Detector%20reduce.png (visited on 04/07/2020).

[3] *Atlas Experiment - Discover the Detector*. URL: https://atlas.cern/discover/detector (visited on 04/07/2020).

[4] *Atlas Experiment - Discover the Detector*. URL: https://cds.cern.ch/images/CERN-GE-0803014-01 (visited on 04/07/2020).

[5] "ATLAS liquid argon calorimeter: Technical design report" (1996).

[6] Manfred Böhm, Ansgar Denner, and Hans Joos. *Gauge theories of the strong and electroweak interaction*. B. G. Teubner, 2001. DOI: 10.1007/978-3-322-80160-9.

[7] Vasiliki Mitsou. "The ATLAS Transition Radiation Tracker". *Particle and Space Physics, Detectors and Medical Physics Applications*. 2003. DOI: 10.1142/9789812702708_0073.

[8] Michael E. Peskin and Daniel V. Schroeder. *An Introduction to quantum field theory*. Addison-Wesley, 1995.

[9] J. J. Sakurai and Jim Napolitano. *Modern Quantum Mechanics*. 2nd ed. Cambridge University Press, 2017. DOI: 10.1017/9781108499996.

[10] M. Tanabashi et al. "Review of Particle Physics". *Phys. Rev. D* 98 (3 2018), p. 030001. DOI: 10.1103/PhysRevD.98.030001. URL: https://link.aps.org/doi/10.1103/PhysRevD.98.030001.

[11] C. S. Wu et al. "Experimental Test of Parity Conservation in Beta Decay". *Phys. Rev.* 105 (4 1957), pp. 1413–1415. DOI: 10.1103/PhysRev.105.1413.

A Appendix: Theoretical Backgound

A.1 Transverse Momentum

Notation We use units where $c = 1$ and we denote four momenta by $\boldsymbol{p}$, three-momenta are denoted by $\vec{p}$ and we will use $p := |\vec{p}|$.

Pseudorapidity Since within the data the energy of the particle and its pseudorapidity is given we need to find a way to determine the transverse momentum, which is done using the relation derived in the following. The pseudo-rapidity, which is used as a measure for the angle between the particles momentum and the beam-axis, is defined as

$$\eta = -\ln\left[\tan\left(\frac{\theta}{2}\right)\right],$$

where θ is the actual angle between the particles momentum and the beam-axis. This can be reexpressed, by geometric constructions, using the longitudinal projection of the momentum of the particle yielding

$$\eta = \frac{1}{2}\ln\left(\frac{p + p_{\mathrm{L}}}{p - p_{\mathrm{L}}}\right).$$

Due to the high energies E of the observed electrons in comparison with their small mass m we can use the following approximations

$$\begin{aligned} m^2 &= \boldsymbol{p}^\mu \boldsymbol{p}_\mu = E^2 - p^2 \\ \Longrightarrow p^2 &= E^2 - m^2 \approx E^2 \\ \Longrightarrow p &\approx E \end{aligned}$$

Such that the pseudorapidity becomes the rapidity y often used in experimental particle physics

$$\eta \approx y = \frac{1}{2}\ln\left(\frac{E + p_{\mathrm{L}}}{E - p_{\mathrm{L}}}\right).$$

We then solve for the energy E, using

$$\begin{aligned} \cosh\eta &= \frac{1}{2}\left(\mathrm{e}^{\eta} + \mathrm{e}^{-\eta}\right) \\ &= \frac{1}{2}\left(\sqrt{\frac{E + p_{\mathrm{L}}}{E - p_{\mathrm{L}}}} + \sqrt{\frac{E - p_{\mathrm{L}}}{E + p_{\mathrm{L}}}}\right) \\ &= \frac{E}{\sqrt{E^2 - p_{\mathrm{L}}^2}} = \frac{E}{p_{\mathrm{T}}} \end{aligned}$$

where we used $E^2 \approx p^2 = p_{\mathrm{T}}^2 + p_{\mathrm{L}}^2$. Hence we can use

$$p_{\mathrm{T}} \approx \frac{E}{\cosh\eta},$$

which is a very good approximation for our purposes.

B Appendix: Higgs Search

B.1 Histograms: Transverse Momenta

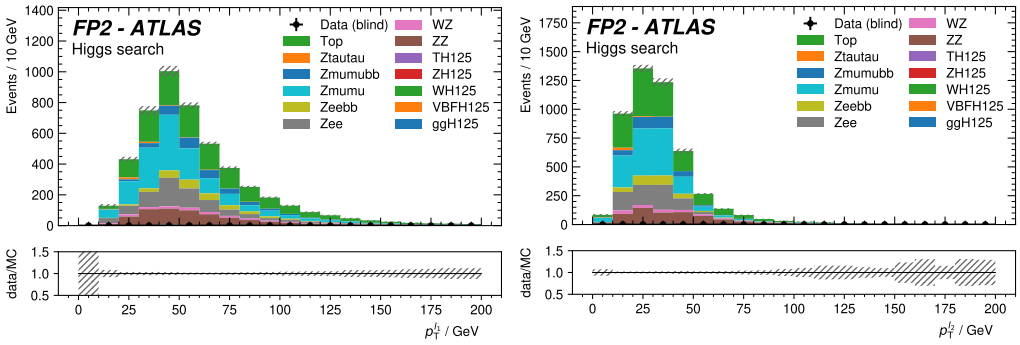

(a) Transverse Momentum of Lepton 1

(b) Transverse Momentum of Lepton 2

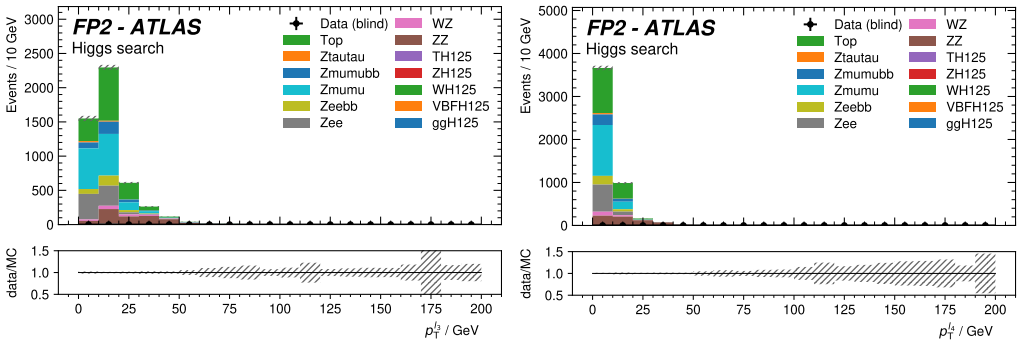

(c) Transverse Momentum of Lepton 3

(d) Transverse Momentum of Lepton 4

Figure 34: In this figure the transverse momentum distributions for each individual lepton are shown, where no cuts are applied.

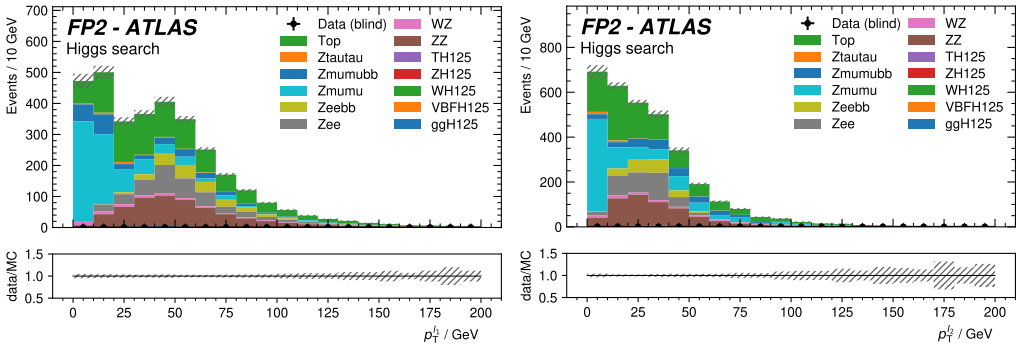

(a) Transverse Momentum of Lepton 1

(b) Transverse Momentum of Lepton 2

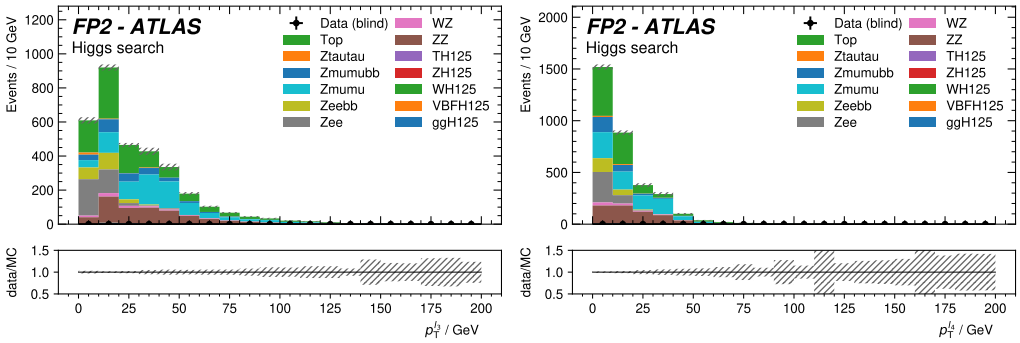

(c) Transverse Momentum of Lepton 3

(d) Transverse Momentum of Lepton 4

Figure 35: In this figure the transverse momentum distributions for each individual lepton are shown, where only the cuts on the lepton number and the total charge of the measured final state are applied.

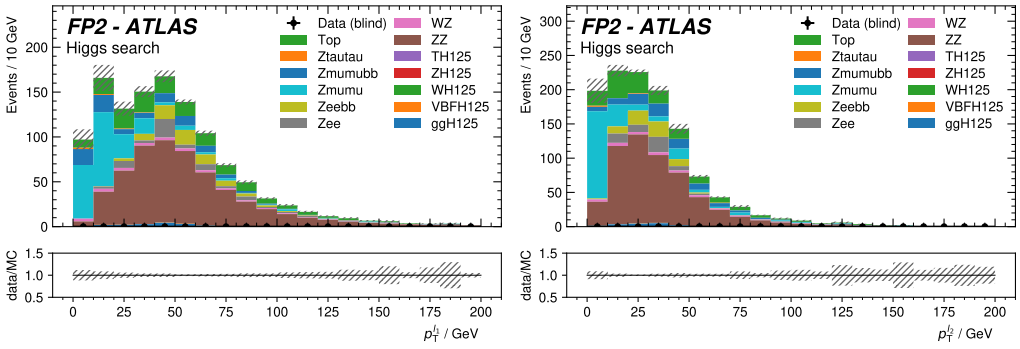

(a) Transverse Momentum of Lepton 1

(b) Transverse Momentum of Lepton 2

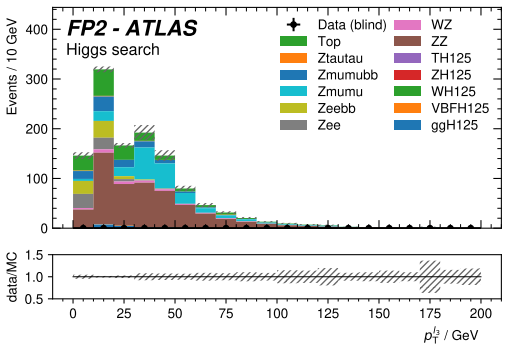

(c) Transverse Momentum of Lepton 3

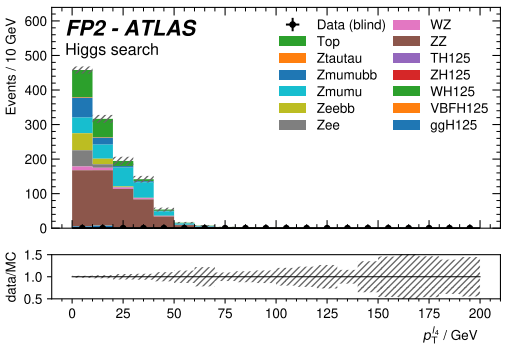

(d) Transverse Momentum of Lepton 4

Figure 36: In this figure the transverse momentum distributions for each individual lepton are shown, where the cuts on the lepton number, the total charge of the measured final state and on the isolation parameters are applied.

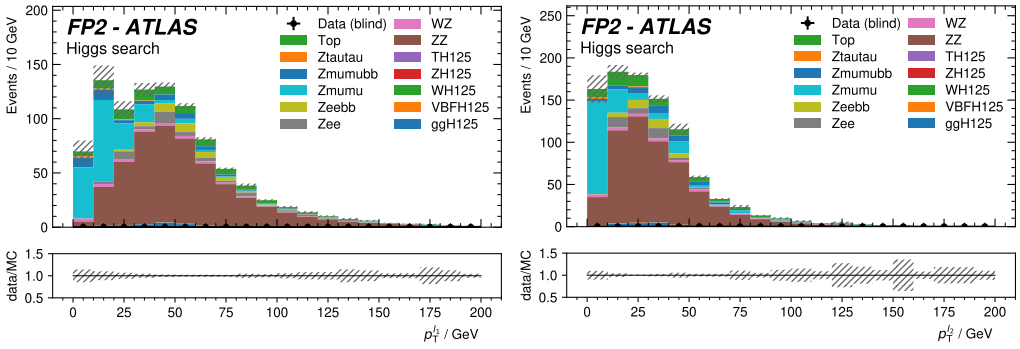

(a) Transverse Momentum of Lepton 1

(b) Transverse Momentum of Lepton 2

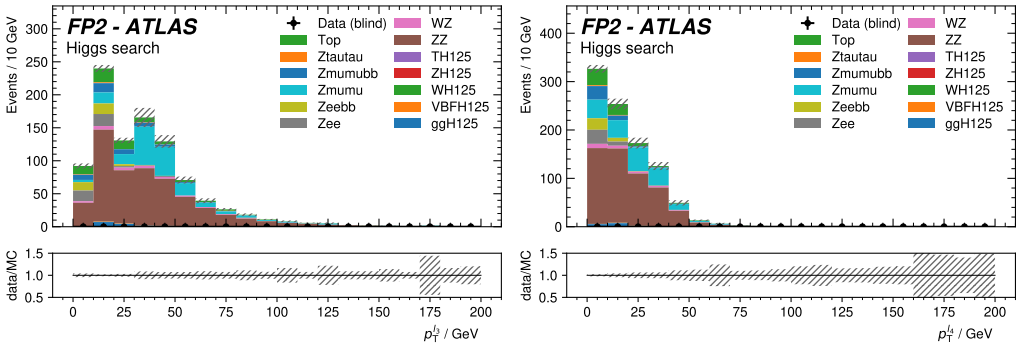

(c) Transverse Momentum of Lepton 3

(d) Transverse Momentum of Lepton 4

Figure 37: In this figure the transverse momentum distributions for each individual lepton are shown, where the cuts on the lepton number, the total charge of the measured final state, the isolation parameters and the impact parameter significances are applied.

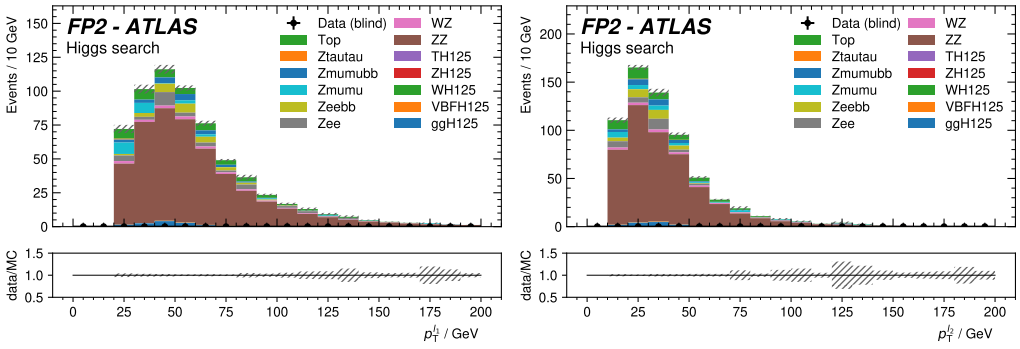

(a) Transverse Momentum of Lepton 1

(b) Transverse Momentum of Lepton 2

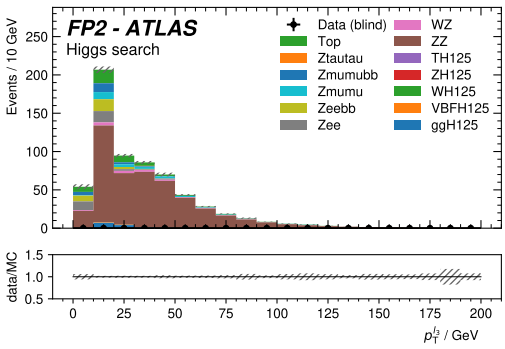

(c) Transverse Momentum of Lepton 3

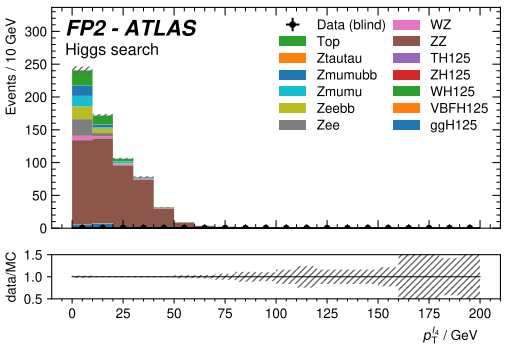

(d) Transverse Momentum of Lepton 4

Figure 38: In this figure the transverse momentum distributions for each individual lepton are shown, where the cuts on the lepton number, the total charge of the measured final state, the isolation parameters, the impact parameter significances and transverse momenta are applied.

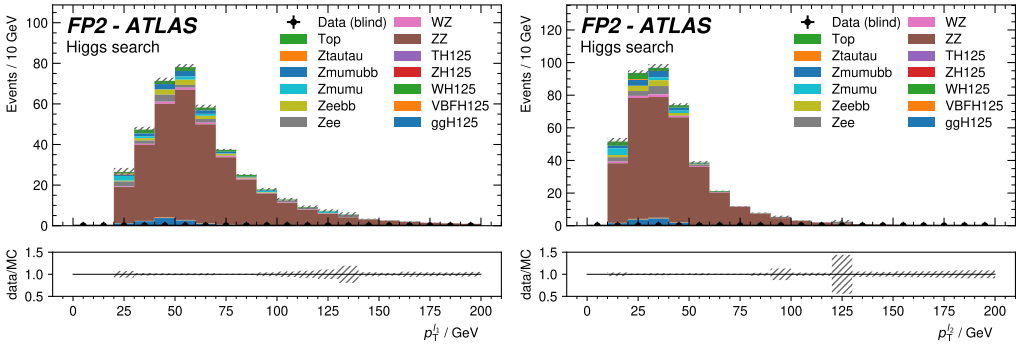

(a) Transverse Momentum of Lepton 1

(b) Transverse Momentum of Lepton 2

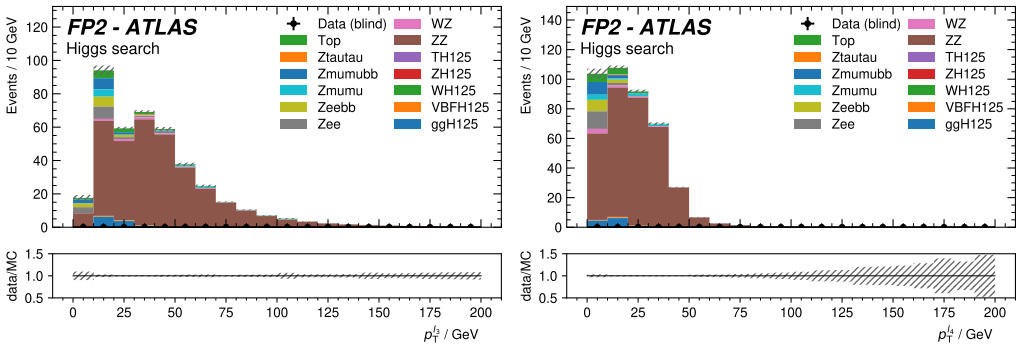

(c) Transverse Momentum of Lepton 3

(d) Transverse Momentum of Lepton 4

Figure 39: In this figure the transverse momentum distributions for each individual lepton are shown, where the cuts on the lepton number, the total charge of the measured final state, the isolation parameters, the impact parameter significances, transverse momenta and invariant masses m_{12}, m_{34} are applied.

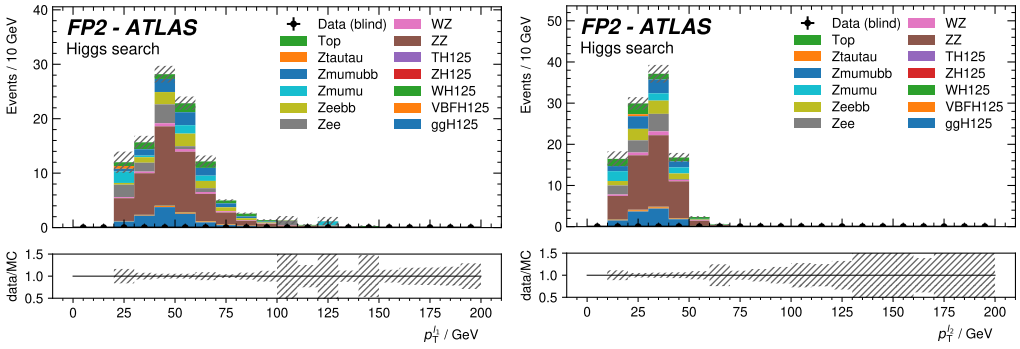

(a) Transverse Momentum of Lepton 1

(b) Transverse Momentum of Lepton 2

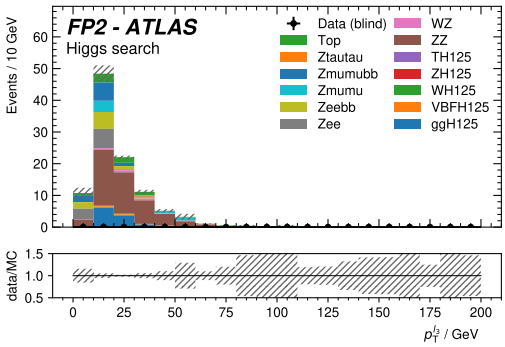

(c) Transverse Momentum of Lepton 3

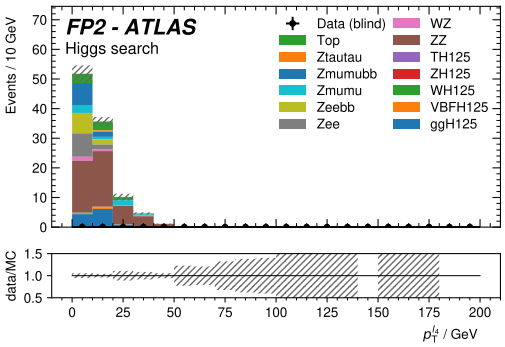

(d) Transverse Momentum of Lepton 4

Figure 40: In this figure the transverse momentum distributions for each individual lepton are shown, where the all chosen cuts are applied. It is seen, that especially the Higgs production via gluon fusion is very present.

B.2 Significance Plots for m_{4l}-Data.

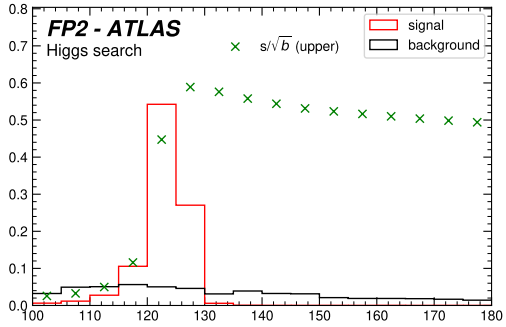

(a) Cuts on: Lepton Number and Charge

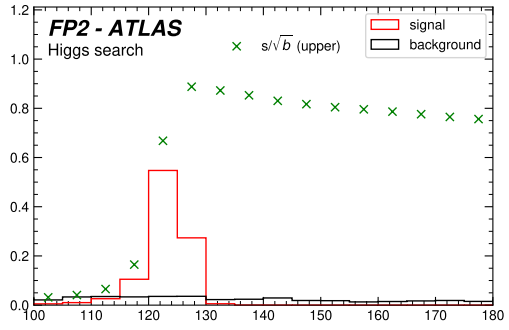

(b) Cuts on: Lepton Number, Charge and Isolation Parameters

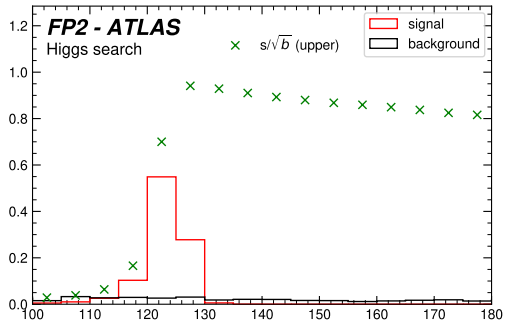

(c) Cuts on: Lepton Number, Charge, Isolation Parameters and Impact Parameter Significance

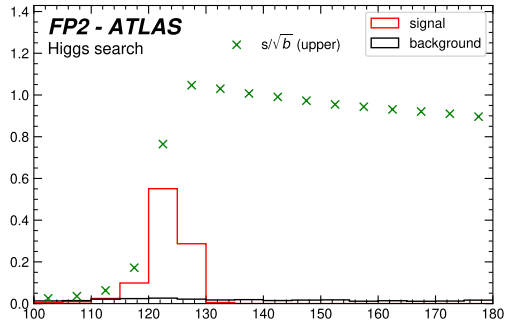

(d) Cuts on: Lepton Number, Charge, Isolation Parameters, Impact Parameter Significance and Transverse Momenta

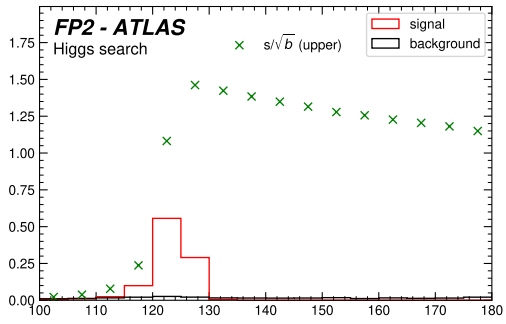

(e) Cuts on: Lepton Number, Charge, Isolation Parameters, Impact Parameter Significance, Transverse Momenta and Invariant Masses m_{12}, m_{34}.

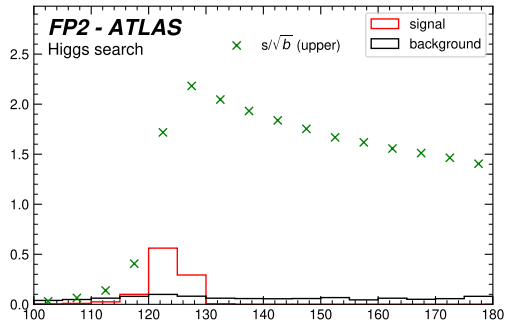

(f) Cuts on: Lepton Number, Charge, Isolation Parameters, Impact Parameter Significance, Transverse Momenta, Invariant Masses m_{12}, m_{34} and Invariant Mass m_{4l}.

Figure 41: In this figure the evolution of the signal significance is displayed.

B.3 Histograms: Invarant Mass

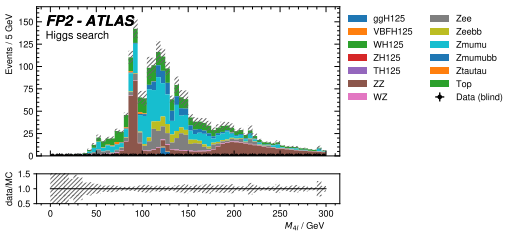

(a) Cuts on: Nothing.

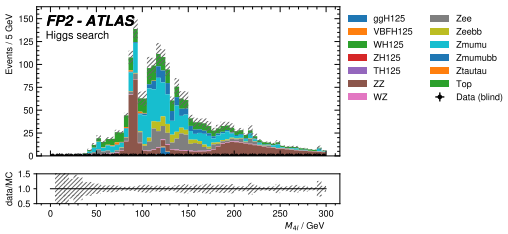

(b) Cuts on: Lepton Number and Charge.

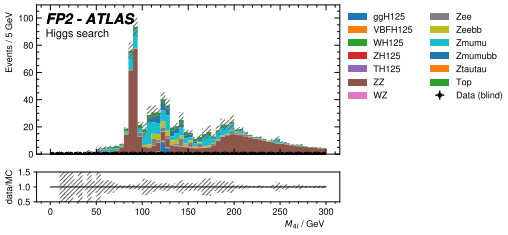

(c) Cuts on: Lepton Number, Charge and Isolation Parameters.

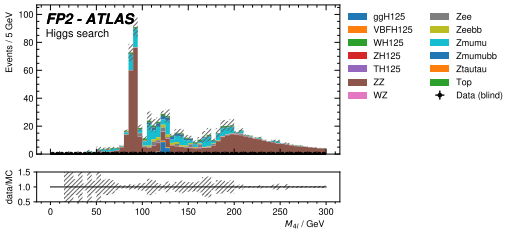

(d) Cuts on: Lepton Number, Charge, Isolation Parameters and Impact Parameter Significance.

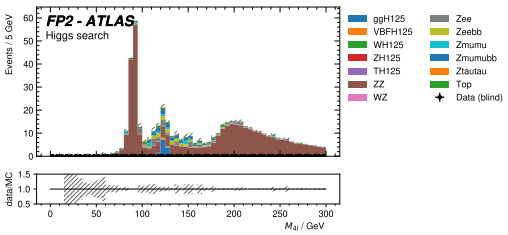

(e) Cuts on: Lepton Number, Charge, Isolation Parameters, Impact Parameter Significance and Transverse Momenta.

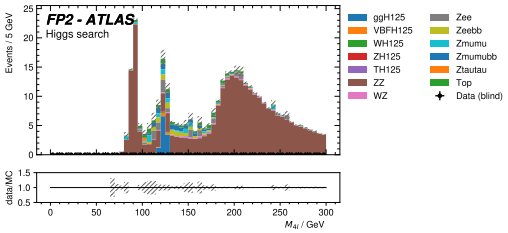

(f) Cuts on: Lepton Number, Charge, Isolation Parameters, Impact Parameter Significance, Transverse Momenta and Invariant Masses m_{12}, m_{34}.

Figure 42: In this figure the evolution of the m_{4l} histogram is displayed. The histogram, where all cuts are applied is found below (fig. 43).

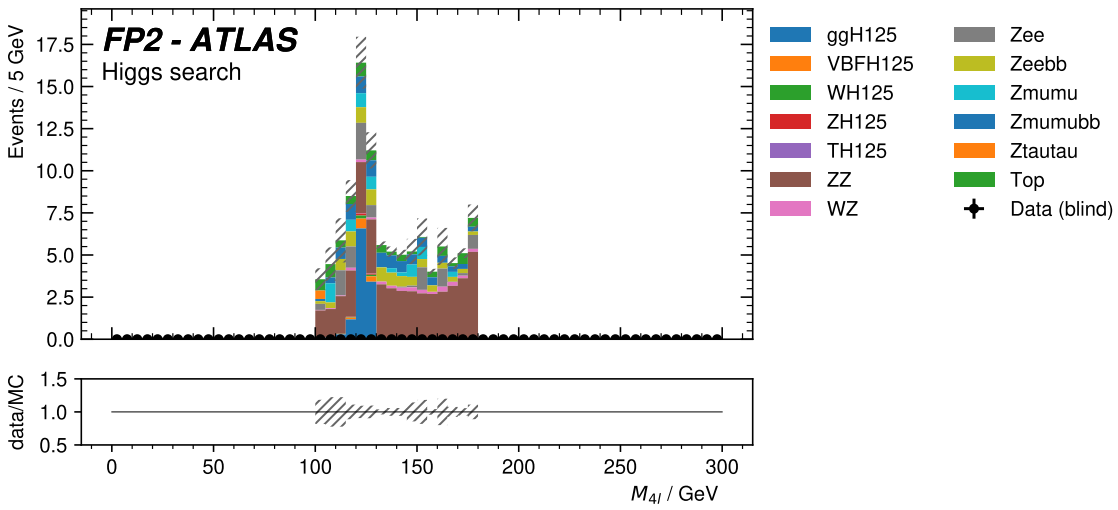

Figure 43: Cuts on: Lepton Number, Charge, Isolation Parameters, Impact Parameter Significance Transverse Momenta, Invariant Masses m_{12}, m_{34} and Invariant Mass m_{4l}.